Band Selection Using 3D Region Growing Algorithm For Hyperspectral Image Analysis

by

Gulnaz Zhambulova

Submitted to the Department of Computer Science
in partial fulfillment of the requirements for the degree of

Master of Science in Computer Science

at the

NAZARBAYEV UNIVERSITY

June 2024

Author . . . .
Department of Computer Science
May 2024

Certified by. . . . .
Dr. Martin Lukac
Associate Professor
Thesis Supervisor

Certified by. . . . .
Dr. Benjamin Tyler
Associate Professor
Thesis Supervisor

Accepted by . . . .
Yelyzaveta Arkhangelsky
Acting Dean, School of Engineering and Digital Sciences

Band Selection Using 3D Region Growing Algorithm For Hyperspectral Image Analysis

by

Gulnaz Zhambulova

Submitted to the Department of Computer Science
on May 2024, in partial fulfillment of the
requirements for the degree of
Master of Science in Computer Science

Abstract

Advancements in sensor technology have significantly increased the importance of hyperspectral imaging (HSI) in various computer vision applications for remote sensing. Modern HSI sensors provide unmatched spectral resolution by capturing images from satellites and drones, encompassing the electromagnetic spectrum from 400 to 2500 nanometers. This study explores how to use the abundant spectral data effectively, specifically addressing the issue caused by the high dimensionality of HSI data. We propose a new method that improves the selection of spectral bands for better segmentation accuracy through the use of a 3D Region Growing Algorithm (RGA). Unlike other selection methods that primarily identify statistically distinct bands, our approach focuses on heuristically searching for the most informative bands. This approach introduces a flexible stopping rule dependent on seed pixel intensity, providing precise control over segmentation by adjusting to different image contrasts. Our approach combines spatial and spectral information to achieve context-aware segmentation. This method has been proven to be effective in various datasets like Salinas, Indian Pines, Pavia Centre, and a real-world dataset, showing its potential in remote sensing.

Thesis Supervisor: Dr. Martin Lukac
Title: Associate Professor

Thesis Supervisor: Dr. Benjamin Tyler
Title: Associate Professor

Acknowledgments

I would like to express my deepest gratitude to my supervisor, Dr. Martin Lukac, whose support, guidance, patience, and trust made my graduate experience exceptionally enjoyable. Your mentorship not only improved my professional skills but also greatly contributed to my personal development, making me a more confident researcher and thinker. You are the one whom others can always approach for new ideas on experiments and projects. Thank you for sparking my interest in research and for taking me on as a research assistant back in 2020. I am very grateful for your support of my aspirations to pursue a PhD. Hopefully, we will publish another paper soon :) I will definitely miss our weekly meetings, the occasional dinners, and the sweets from Japan.

My sincere thanks also go to my dear lab-mates, Zhamilya and Jamilya, for sharing this research journey with me. Thank you for being there in the lab, for the warm conversations about everything and everyone, and for sharing the burden of uncertainty that accompanies many graduates.

Additionally, I must acknowledge the role of my family, who provided me with moral support throughout my studies and was always understanding when I was busy with studies. I am particularly thankful to my husband for his love, encouragement, and belief in me — often more than I believed in myself. Thank you for being there through all my tears and stress as deadlines approached.

Lastly, I cannot forget to thank the friends from "Ozimiz otyryp sharap isheik," who were there for me throughout the entire process. I am truly thankful for all their support and for making the journey enjoyable and memorable.

Contents

5 Conclusion **51**

List of Figures

List of Tables

Chapter 1

Introduction

Over the past few decades, advancements in modern sensor technology have significantly increased the importance of hyperspectral imaging in various computer vision tasks. Hyperspectral Images (HSI) are mostly captured from satellites, aircraft, and drones. Modern HSI sensors have a spectral resolution ranging from 2 to 20 nanometers, while covering electromagnetic spectrum with a wavelength between 400 and 2500 nanometers [1]. This chapter introduces the research topic by outlining the motivation for the study, defining the research problem, and providing an overview of the proposed solution.

1.1 Motivation

The difference of HSI from ordinary RGB images is its ability to provide a notably greater amount of spectral information. This is because each pixel represents a high-dimensional vector, usually comprising reflectance data from hundreds of closely spaced, narrow-band spectral channels. HSI covers a wide spectrum that includes infrared, visible, and sometimes ultraviolet light. Thus, these images can reveal details about objects that are invisible to the naked eye, such as chemical compositions or thermal conditions [2]. This attribute makes HSI invaluable in fields such as agriculture, food quality assessment, mineralogy, medical imaging, art conservation, among other areas [3, 4, 5, 6, 7, 8].

Research shows that different materials reflect, transmit, and absorb light in unique ways, giving each a distinctive spectral signature [9]. Thanks to the high spectral resolution of HSI, it is possible to distinguish even very similar objects within the same category, such as different sub-types of trees or rocks. For example, Figure 1-1 illustrates the spectral signatures of different types of Broccoli and Fallow classes. These signatures were obtained by averaging all pixels associated with a specific type within the Salinas dataset. For the classes "broccoli_green_weeds_1" and "broccoli_green_weeds_2", a noticeable difference in spectral curves can be observed in the near-infrared range. Meanwhile, for the two sub-types of the Fallow class — namely, "fallow_rough_plow" and "fallow_smooth" — the difference is significant across the entire spectral range.

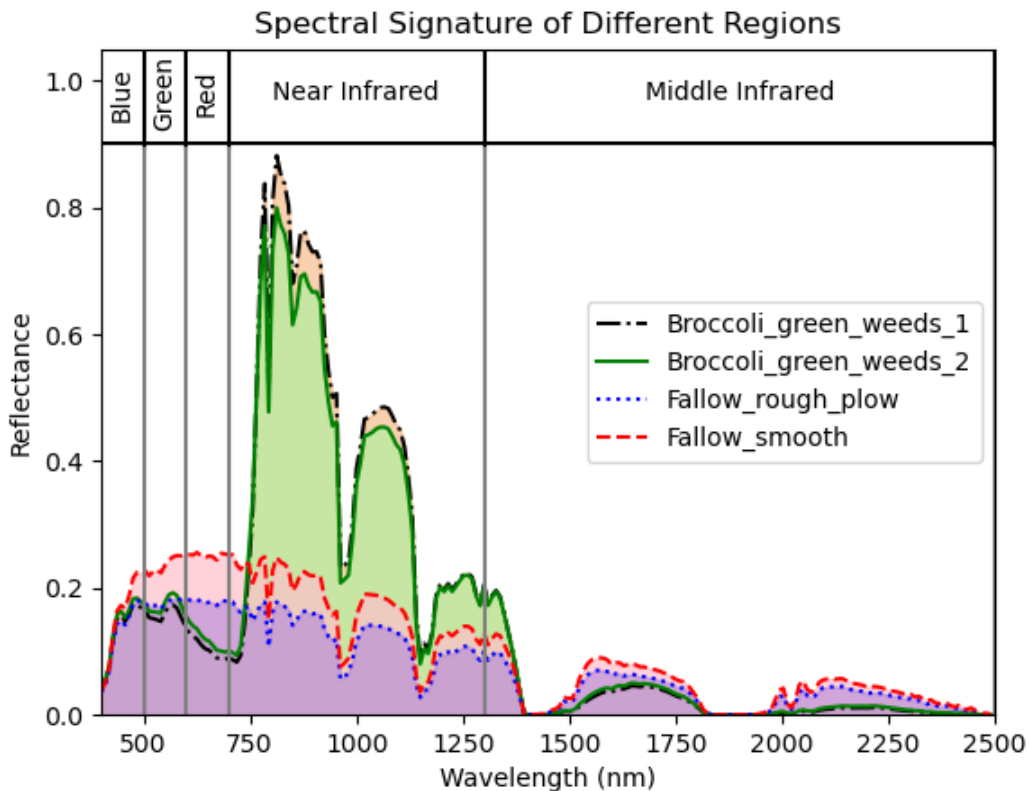

Figure 1-1: Spectral signatures of Brocoli and Fallow classes from Salinas Dataset.

Moreover, HSI enables the detection of changes in the spectral signature of materials that may be caused by external factors such as environmental conditions or

biological stressors [10]. Therefore, HSI can be used not only for material identification but also for monitoring environmental changes or detecting early signs of disease in crops and natural ecosystems. By analyzing these spectral signatures over time, experts can make informed decisions and implement timely interventions.

1.2 Problem Statement

In HSI analysis, traditional segmentation and classification methods often struggle to efficiently and accurately exploit the rich spectral-spatial information contained within the data. This is because of the high dimensionality of HSI and the variability in spectral signatures across different materials [8]. Therefore, a crucial preliminary step in the analysis of HSI data involves the reduction of its dimensionality [9]. This step is designed to remove spectral redundancies while preserving vital information for subsequent analysis.

There are two primary types of techniques for reducing the dimensionality of HSI data: band selection and feature extraction. Feature extraction transforms the original dataset into a new set of features based on certain criteria, typically involving linear combinations of all original bands [11]. However, this method offers a low interpretability. Interpretability is essential for applications requiring precise identification, such as agriculture, environmental monitoring, and urban planning. On the other hand, the band selection technique chooses specific bands from the original dataset, preserving the spectral relevance of the channels [12].

Yet, existing band selection techniques often fail to identify the most informative spectral bands accurately, resulting in sub-optimal outcomes. These methods usually prioritize statistically distinct bands, possibly overlooking less prominent bands that contain crucial information for specific tasks [12]. Moreover, these techniques tend to generalize poorly to datasets for which they were not specifically designed [13]. Additionally, they often neglect the importance of continuity and correlation between adjacent spectral bands, which are crucial for forming the spectral signature of objects [14].

1.3   Proposed Approach

To overcome the limitations of existing band selection techniques, this study presents a novel method that employs a 3D Region Growing Algorithm (RGA). The method strategically searches for the most informative spectral bands by evaluating the accuracy of 3D RGA segmentation across different bands. Segmentation starts from a predefined seed point and grows until it meets a unique stopping criterion. This criterion dynamically adjusts based on the intensity of a seed pixel, bounded by a fraction of the average pixel intensity of the entire image. With such flexible control over the region growing process, the algorithm can adapt to varying levels of signal strength across different parts of the HSI. Moreover, the method uses a 3D framework to analyze both spatial and spectral information, resulting in more context-aware segmentation compared to traditional 2D approaches.

Through our experiments across several datasets, including Salinas, Indian Pines, Pavia Centre, and NERC-ARF, we demonstrate the effectiveness and adaptability of our approach. The experiments highlight the spectral continuity and correlation within the electromagnetic spectrum, with a range of bands emerging as most informative for all classes under study. Moreover, these experiments show that even vegetation types that appear similar may have distinct informative spectral bands. However, the method may not perform as well in handling small, non-homogeneous regions.

By using the most informative bands identified in our experiments, the process of identifying regions of interest can be simplified to focusing only on these specified bands and neglecting the rest. By concentrating on the most informative bands, experts can avoid the tedious task of examining hundreds of bands, thus accelerating the information retrieval process and improving accuracy. Thus, our approach not only addresses the challenge of high dimensionality in HSI but also helps experts to detect anomalies in the spectral signature more efficiently.

Chapter 2

Related works

Currently, numerous studies are focusing on applying machine learning and Deep Learning (DL) techniques for extracting the most useful spectral information. This focus stems from the challenge posed by high-dimensional data with which the accuracy of models tends to decrease — a phenomenon known as the curse of dimensionality or Hughes phenomenon [15]. As reducing dimensionality is a critical step in HSI analysis, this section of the thesis delves into previous research related to spectral feature extraction and band selection. It concludes with a discussion on the principles and applications of the RGA.

2.1 Spectral Feature Extraction Methods

Spectral Feature Extraction (SFE) methods can be classified as supervised or unsupervised, based on the necessity of training data, and as shallow or deep, depending on the use of DL techniques [16, 11].

2.1.1 Shallow Feature Extraction Methods

One of the most commonly used unsupervised shallow SFE method is Principal Component Analysis (PCA) [17, 18]. PCA is designed to transform HSI data into a lower-dimensional space. It does this by projecting the original data onto a new

set of orthogonal axes that maximize variance and minimize redundancy among features. Various adaptations of PCA have been developed specifically for handling HSI data [19], among which the Maximum Noise Fraction (MNF) is considered more effective than the standard PCA [20, 21, 22]. Unlike PCA, MNF focuses on maximizing the Signal-to-Noise Ratio (SNR), thereby effectively managing the noise variations across different spectral bands. Another notable shallow SFE method is Independent Component Analysis (ICA) [23]. ICA aims to separate the original dataset into independent non-Gaussian components through an unmixing matrix. It can identify even minor material differences. It is especially useful when PCA struggles due to insufficient samples to construct reliable statistics because of its dependence on second-order statistics [24, 25].

By adding kernel functions, the aforementioned methods can address non-linearity in HSI data. As a result, variations such as kernel-PCA [26], kernel-MNF [27], and kernel-ICA [28] have been developed. The effectiveness of such techniques relies on the selection of the kernel function and the accurate estimation of parameters [11]. On the other hand, manifold learning techniques focus on the exploration of local geometric relationships within the feature space [16]. Thus, they offer a more detailed understanding of data structure and show superior performance in handling non-linear data [29]. ISOMAP, for instance, constructs a neighborhood graph, calculates the shortest paths within this graph, and generates lower-dimensional embeddings that preserve these path distances [30].

Wavelet Transform (WT), usually used in signal processing, represents another category of SFE methods. Its main idea is to analyze a signal at different frequencies with varying resolutions [31]. The 1D Discrete WT is commonly used for spectral reduction in HSI data [32]. However, recently WT is extended to 3D [33], used with graph-based methods [34], and with DL techniques such as Convolutional Autoencoders [35] and Convolutional Neural Networks [36].

Well-known example of supervised shallow SFE method is Linear Discriminant Analysis (LDA) and its variants such as Regularized LDA, Local Fisher's Discriminant Analysis, Graph-based and Kernelized Discriminant Analysis [37]. These methods

18

derive low-dimensional representations from data by establishing various supervised rules based on data label. However, in the context of HSI feature extraction, DL methods have gained importance for their effectiveness in recent studies [38].

2.1.2   Deep Feature Extraction Methods

DL methods autonomously learn complex features directly from raw data through hierarchical layers, offering more distinctive, abstract, and stable features compared to shallow techniques [16]. Autoencoders (AEs) and Convolutional Neural Networks (CNNs) stand out as particularly favored models within DL for HSI analysis.

AE typically comprises two main components: an encoder that transforms the input vector into a hidden representation and a decoder that aims to reconstruct the original input [39]. It can be used within different learning frameworks. For example, the AE with hypergraph structure as its backbone is adapted both for unsupervised and semi-supervised classification of HSI [40]. AEs are also commonly employed in simultaneous analysis of spectral and spatial information. For example, Variational AE is used for extracting spectral-spatial features in unsupervised manner in [41]. Another approach combines superpixel-based and band-based similarity graphs within the AE to effectively use both spectral and spatial information [42].

CNNs, particularly well-suited for image recognition and processing, are widely used for HSI feature extraction. Although they can be implemented in an unsupervised framework [43, 44], they are more commonly applied in supervised settings. The recent trend towards 3D CNNs aims to extract both spectral and spatial features from HSI data, though at the cost of increased training complexity and a higher risk of overfitting [45, 46]. To mitigate these issues, hybrid methods combining 2D and simplified 3D CNNs have been proposed [47, 48].

Furthermore, the integration of multiple DL networks has shown promising results in HSI analysis. For instance, a network with Long Short-Term Memory (LSTM) and Deep Neural Network (DNN) within the AE framework has been used for nonlinear HSI unmixing [49]. Another study employed a Stacked AE for unsupervised feature learning, followed by a 3D Deep Residual Network (ResNet) for classification [50].

19

The combination of CNNs with Graph Convolutional Networks (GCNs) exploits both pixel-level and superpixel-level features [51]. Moreover, a pair of CNN and LSTM integrates extraction of spatial and spectral features simultaneously [52].

These feature extraction methods transform the initial dataset into a new set of features through linear or nonlinear combinations of original bands, based on specific criteria. However, such an approach may complicate outcome interpretation if the criteria for feature selection are not clearly defined. As a result, when interpretability is crucial, band selection methods are often preferred for dimensionality reduction.

2.2   Spectral Band Selection Methods

In Band Selection (BS) methods, the selected bands preserve their original physical meaning, making it easier to interpret the information for specific applications. BS methods can be categorized into ranking-based, search-based, clustering-based, sparsity-based, embedding-learning based, and hybrid-scheme based methods based on their underlying approach [12, 14]. Notably, ranking-based, clustering-based, and some search-based methods operate under an unsupervised framework [53].

Ranking-based approaches evaluate the significance of each spectral band based on a predetermined criterion for band prioritization and choose the highest-ranking bands in an ordered sequence [54]. For band ranking these methods typically use information metrics such as divergence, entropy, or mutual information, distance-based metrics including Bhattacharya distance, Kullback–Leibler divergence, Jeffries–Matusita distance, Hausdorff distance, or Spectral Angle Mapper (SAM), and dependency metrics measuring correlation and similarity [55]. For instance, a similarity-based ranking strategy employs the structural similarity index to measure the similarity between band pairs [56]. Another criterion, Self-Mutual Information (SMI), evaluates the unique information a single band contributes compared to the entire dataset [57]. Additionally, the Band Ranking via Extended Coefficient of Variation (BRECV) method proposes a criterion for selecting bands based on their relative informativeness, prioritizing those with smaller means and larger standard deviations

relative to adjacent bands [58]. It is also feasible to integrate various ranking measures — such as variance, information entropy, and the Optimum Index Factor (OIF) — for band selection [59].

Clustering-based methods categorize the original bands into groups and choose representative bands from each group to form the final subset [60]. Conventional clustering algorithms, such as the K-means algorithm [61], hierarchical clustering [62], and spectral clustering [63], are widely used for grouping bands. In one approach, adjacent bands are iteratively clustered together using a coarse-fine strategy, with representative bands chosen based on local density and information entropy [64]. Another technique involves generating superpixels — groups of adjacent pixels in an image merged based on similar characteristics — as a preprocessing step. The Simple Linear Iterative Clustering (SLIC) method is used for superpixel generation in [65], followed by clustering with band selection criteria derived from the Relevant Component Analysis (RCA) algorithm. The Entropy Rate Superpixel (ERS) segmentation technique, combined with K-means clustering, also demonstrates comparable effectiveness [66].

Searching-based methods approach band selection as the optimization of a specific criterion function, aiming to identify the best bands that constitute an optimal solution [67]. Like ranking-based methods, the criterion function may involve similarity-based or information-based metrics [12]. Recent advancements explore alternative criteria. For instance, one study employs a reconstruction-based objective function to assess a band subset's ability to reconstruct the original dataset [68]. Another work introduces the Maximum Information and Minimum Noise (MIMN) criterion to select bands that maximize information while minimizing noise [69]. Search strategies vary across literature too. For example, a Cuckoo Search algorithm enhanced with a Chebyshev chaotic map initialization is proposed to optimize the search [70]. Additionally, progressive algorithms like genetic algorithms [71] and particle swarm optimization (PSO) [72] have been applied to the band search task.

Sparsity-based band selection methods employ sparse representation or regression to uncover specific underlying patterns within HSI data [73]. In [74], the

selection of a sparse subset is achieved through learning pairwise band agreements, facilitated by a spatial-spectral graph regularizer. Sparse representation can also be obtained using DL networks, such as AEs [75] or CNNs [76]. Commonly, such methods integrate attention mechanism. In [77], the authors process each spectral band independently using band-specific 1x1 convolution kernels. Their model further employs hard thresholding to discard bands with convolution weights below a certain threshold, selecting bands with significant features.

Embedding learning-based methods integrate band selection within the optimization process of specific application models, such as classification or target detection [78]. Various strategies can be employed within this optimization process. For example, one study extracts a subset of bands using optimal neighboring reconstruction, followed by CNN-based classification [79]. Another research applies deep reinforcement learning to determine an optimal band subset that enhances classification accuracy [80]. Similarly, a custom attention network has been developed for selecting bands specifically for maize seed variety identification [81]. Additionally, a novel approach introduces a 3D multiscale reconstruction network with three parallel attention modules to select bands for classification [82].

Recent works in the field usually integrate multiple approaches. For instance, one method addresses the latent low-rank representation optimization problem by calculating sparse coefficients and selecting representative bands through spectral clustering [83]. Another study achieves sparse representation using the attention module of a GCN and incorporates it into a dense GCN for classification [84]. Approaches based on ranking and search are also often merged. For example, one technique employs 3D Discrete Cosine Transform-based information entropy for ranking and the Sequential Forward Selection algorithm for searching [85]. Moreover, a deep transform model coupled with K-means combines clustering-based features with embedding-learning techniques [86]. Embedding-learning methods can also work together with search methods by merging CNN with genetic algorithms [87].

Integrating advanced ML with spectral band selection introduces new opportunities but faces challenges. Many algorithms are designed to work well with certain

types of data, which limits their ability to be effective in various areas [13]. Such methods often prioritize bands with significant statistical differences, potentially neglecting bands crucial for specific tasks [12]. Moreover, they tend to disregard the importance of the relationship among neighboring spectral bands, crucial for generating spectral signatures [14]. As a result, existing band selection techniques may fail to identify the most informative bands, resulting in suboptimal segmentation outcomes.

2.3 Region Growing Algorithm

Region Growing Algorithm (RGA) works by expanding a region from a chosen starting point, or seed, by including neighboring pixels that are similar to the seed. This approach was initially introduced in 1994 by Adams and Bischof [88]. The algorithm is particularly popular in the field of medical imaging, where it is often applied for segmenting organs or identifying cancerous tissues [89, 90, 91].

Table 2.1: Region Growing Algorithm in literature

Cite	Image type	Aim	Seed selection	Stopping criteria
[92]	UAV imagery	Tree crowns delineation	A local maxima approach	Euclidean distance < thershold
[93]	DEM	Identification of valleys	Manual	$|$Pixel-Seed$|$ < 0.02
[94]	DEM	Under-vegetation flood detection	Water level measurements	$Elevation\_pixel >= Elevation\_seed$
[95]	3D point cloud	Class-agnostic point cloud segmentation	Minimum curvature	Learnable parameter from deep neural network
[96]	HSI	HSI classification	Random from ROI	Confidence of CNN classification
[97]	UAV imagery	Tree crown delineation	Manual	Spectral difference and distance decay
[98]	HSI	HSI classification	Random from ROI	Confidence of CNN classification
[99]	HSI	Painting segmentation	Superpixels	Kernel SAM
[100]	VHR images	Semantic segmentation	Random from ROI	Confidence of CNN classification
[101]	Grayscale images	Identification of cracks in tunnels	Local threshold segmentation	$(n+2)P/(n+1)P\_seed <$ threshold
[102]	DEM	Extraction of terrain shoulder lines	Calculated flow direction and slope	Difference in terrain slope and topographic position index

The adaptability of the RGA across various applications make it a widely used tool in the remote sensing field. Table 2.1 summarizes recent studies that have implemented the RGA in remote sensing, employing a diverse range of image modalities

from ordinary grayscale images to HSI. Grayscale imagery has been employed to identify cracks in concrete tunnel linings [101]. Unmanned Aerial Vehicle (UAV) imagery, known for providing high-resolution images of the Earth's surface, has been used for delineating tree crowns [92, 97]. The Digital Elevation Model (DEM), which offers 3D representations of a terrain's surface, is applied in the identification of valleys, under-vegetation flood detection, and delineation of terrain shoulder lines [93, 94, 102]. Additionally, one study used 3D point clouds for class-agnostic point cloud segmentation [95], where a point cloud refers to data points generated by 3D scanners to represent an object's external surface. Very High Resolution (VHR) images have been used for semantic segmentation [100], characterized by their ability to capture the smallest object details with precision. Lastly, HSI has been applied for pixel-wise classification and painting segmentation [96, 98, 99], demonstrating the extensive applicability of RGA in processing remote sensing data.

The initial step in RGA involves the selection of informative and distinctive seed points [103]. Various strategies for seed selection have been explored. Among the simplest and most common methods is manual selection, either by experts [93, 97] or through random choice from a Region of Interest (ROI), aided by ground truth data [96, 98, 100]. Ramli et al. [92] employed a local maxima approach with the assumption that maxima correspond to treetops. Additionally, certain methods incorporate a preprocessing step to calculate specific values, such as water level measurements [94], minimum curvature in a point cloud [95], or water flow direction and slope [102]. Seeds may also be selected from segmented regions via superpixels or local threshold segmentation [99, 101].

The region initiates from specific seed point and expands until meeting predetermined growth criteria [103]. A commonly adopted strategy is to apply a threshold to the difference between the seed point and its neighboring pixels. This difference can be quantified in various ways, including through pixel intensities [93], water elevation values associated with pixel positions [94], or terrain slope and topographic position index [102]. Distance metrics, such as the Euclidean distance [92, 97], and the Kernel Spectral Angle Mapper [99], are also used to facilitate this process. In [101], the for-

mula for the stopping condition is designed to cap the number of iterations n. More recently, the use of DL models has been explored, where these networks are tasked with classifying pixels, and a threshold is then established based on the confidence scores of these classifications [96, 98, 100]. Similarly, encoder-decoder networks have been applied to directly learn the threshold value from the data [95], indicating a shift towards more data-driven methods.

All of the above mentioned studies use 2D RGA. It means that the growth is in spatial dimensions and can happen in 4-connected or 8-connected neighbourhoods as shown in Figure 2-1. If we assume x and y as positions of the seed pixel, the region can grow along the vertical and horizontal directions surrounding the seed pixel (Figure 2-1 (a)). This means growth can occur to the pixels directly above, below, to the left, and to the right of the seed pixel. Moreover, the region can grow along the diagonal axes (Figure 2-1 (b)). This includes the four directions mentioned for 4-connected neighbourhoods, plus the pixels on the diagonal: upper-left, upper-right, lower-left, and lower-right. The 8-connected approach facilitates a more natural, star-shaped expansion, allowing for a comprehensive inclusion of neighboring pixels. Therefore, 8-connected neighbourhood is more common in literature [93, 96, 100, 102].

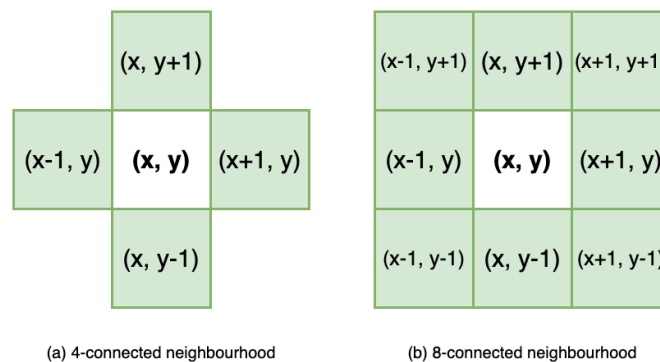(a) 4-connected neighbourhood   (b) 8-connected neighbourhood

Figure 2-1: Growth directions for 2D RGA.

In the field of medical imaging, the segmentation within volumetric data, commonly found in medical scans such as CT or MRI, is performed using 3D RGA [104, 105]. The growth can happen in 6-connected, 18-connected, or 26-connected neighbourhoods as shown in Figure 2-2. This method enhances the traditional 2D RGA by

incorporating a third dimension, depth. 6-connected neighborhood enables growth to the immediate top, bottom, left, right, front, and back voxels (Figure 2-2 (a)). 18-connected neighborhood expands this by including diagonal connections in the same plane and directly adjacent planes (Figure 2-2 (b)). 26-connected neighborhood further extends the connectivity to include voxels that share at least a corner with the central voxel or seed (Figure 2-2 (c)).

(a) 6-connected neighbourhood   (b) 18-connected neighbourhood   (c) 26-connected neighbourhood
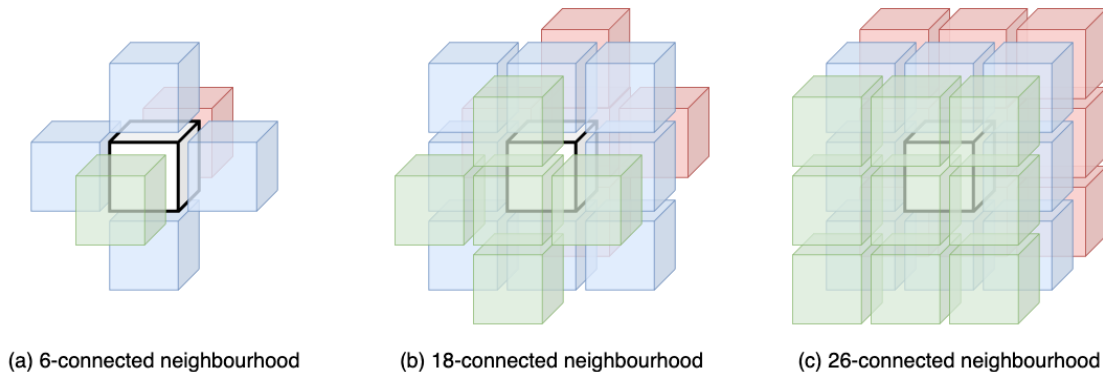
Figure 2-2: Growth directions for 3D RGA.

However, to the best of our knowledge, 3D RGA has not yet been applied to HSI. Given the scarcity of labeled HSI datasets, the fact that RGA does not require training data make it particularly useful for HSI analysis. Furthermore, it operates locally around a selected seed point, allowing it to process the original image directly without discarding any spectral-spatial information. This aspect is particularly advantageous for band selection. The flexibility of the growth criteria allows for easy adaptation to our specific task. By extending 2D RGA to 3D, we can examine the depth of the segmentation and analyze the impact of the spectral dimension. By controlling the spectral band of the seed point, we can select the band from which the region begins to grow, assessing each band's ability to effectively segment relevant features. Therefore, this work employs the 3D RGA to identify the most informative spectral bands for various classes.

Chapter 3

Methodology

This chapter provides a detailed description of the methodology used to identify the most informative spectral bands. As it employs a segmentation-based method, we first describe the 3D Region Growing Algorithm used for segmentation. Subsequently, we introduce the set of evaluation metrics designed to assess "informativeness." The chapter concludes with an overview of the entire process.

3.1   3D Region Growing Algorithm

The flow diagram presented in Figure 3-1 illustrates a 3D Region Growing Algorithm (RGA) applied to segment HSIs for the purpose of identifying the most informative spectral bands. The methodology starts with the selection of a seed pixel within the HSI, characterized by its spatial coordinates (x, y) and a specific spectral band (z). These spatial coordinates are randomly chosen from the Region of Interest (ROI) while considering the ground truth of the datasets. Meanwhile, the spectral band is selected sequentially, ensuring all bands are eventually considered.

Once a seed pixel is chosen, the next step is to select a neighboring pixel from a 6-connected neighborhood. As depicted in Figure 2-2 (a), it is a pattern of connectivity that considers adjacent pixels in 3D space, which share a face with the central pixel. 6-connected neighborhood strategy is used as a trade-off between computational efficiency and the precision of region delineation.
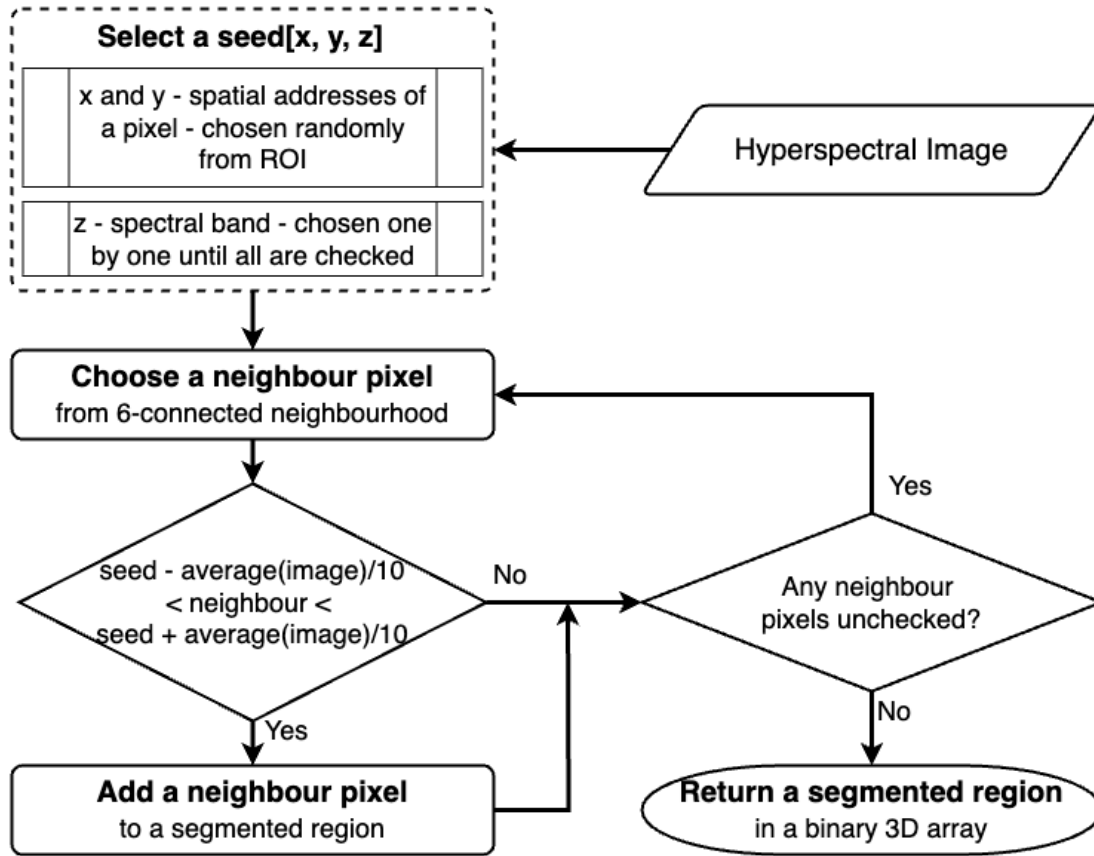
Figure 3-1: Flow diagram of 3D RGA.

The algorithm then evaluates whether the neighbour pixel falls within a specified growth criteria. Specifically, it is checked if the neighbor's value is greater than the seed intensity minus one-tenth of the image's average and less than the seed intensity plus one-tenth of the image's average. If the condition is met, the neighboring pixel is considered similar enough to the seed to be added to the segmented region.

After a neighbor is added to the segmented region, the algorithm checks if there are any unchecked neighboring pixels remaining. If there are, the process iterates, continuing to grow the segmented region by evaluating neighboring pixels. If there are no unchecked neighbor pixels, the process stops. The output of the algorithm is a segmented region represented in a binary 3D array, where the segmented pixels are marked in contrast to the non-segmented, background pixels.

3.2   Evaluation Metrics

To evaluate the informativeness of spectral bands, two metrics are used: Normalized Mutual Information (NMI) and Adjusted Rand Index (ARI). These metrics are commonly employed to assess the accuracy of segmentation methods. In our analysis, to derive NMI and ARI scores, a region segmented from a 3D RGA is compared with the corresponding ground truth region, where a seed pixel originates.

Mutual Information (MI) quantifies the shared information between the two segmentations, providing a measure of similarity between them. MI score between the segmented image and the ground truth is calculated based on their joint and individual probability distributions as shown in Equation 3.1.

$$MI(S,G) = \sum_{i=1}^{|S|} \sum_{j=1}^{|G|} \frac{|S_i \cap G_j|}{N} \log \frac{N|S_i \cap G_j|}{|S_i||G_j|} \tag{3.1}$$

where S is segmentation result and it has $|S|$ number of segmented regions; G is ground truth and it has $|G|$ number of true classes; $|S_i|$ is the number of pixels in segmented region i; $|G_j|$ is the number of the pixels in true class j; $|S_i \cap G_j|$ is number of pixels that are in both i and j; N is the total number of pixels. So, the formula sums values obtained for all pairs of segmented regions and true classes.

NMI is the normalized version of the MI. Normalization is done using the Equation 3.2. Its scale is from 0 to 1, where 0 means no mutual information, and 1 means perfect information sharing.

$$NMI(S,G) = \frac{2 \times MI(S;G)}{H(S) + H(G)} \tag{3.2}$$

where $MI(S;G)$ is the mutual information between segmentation result and ground truth; $H(S)$ and $H(G)$ are entropy of S and G.

Rand Index (RI) also provides a measure of similarity between two data segmentations. It measures similarity by assessing every possible pair of pixels in the image, as shown in Equation 3.3. Each pixel pair from the segmentation result may either be in the same segmented region or in separate regions. Similarly, pixel pairs from

the ground truth may either belong to the same class or to different classes. Thus, the RI calculates the proportion of pixel pair agreements — those belonging to the same or to different classes in both the segmentation result and the ground truth — relative to the total number of pixel pairs.

$$RI = \frac{TP + TN}{TP + FP + FN + TN} \qquad (3.3)$$

where given S is the segmentation result and G is the grounf truth, TP (True Positive) is the number of pixel pairs that are in the same region in both G and S; TN (True Negative) is the number of pixel pairs that are in different regions in both G and S; FP (False Positive) is the number of pixel pairs that are in the same region in S but in different regions in G; FN (False Negative) is the number of pixel pairs that are in different regions in S but in the same region in G.

The original RI's limitation is it does not account for the possibility of achieving a high score by chance, especially in situations with a large number of clusters or when cluster sizes are uneven. The ARI adjusts the RI by considering the expected similarity of all pairings under random classification, as depicted in Equation 3.4. This normalization ensures that the ARI can give a score that is more indicative of the actual agreement between two clusterings, beyond what would be expected by chance. The value of ARI ranges from -1 to 1, where a value of 1 indicates perfect agreement between the two clusterings; a value of 0 suggests that the observed agreement is no better than what would be expected by chance; a value less than -1 indicates agreement that is worse than random chance.

$$ARI = \frac{RI - expected(RI)}{max(RI) - expected(RI)} \qquad (3.4)$$

where $expected(RI)$ is the expected value of the RI if the regions are randomly segmented, calculated based on the distribution of the class sizes; $max(RI)$ is the maximum possible index value, representing the case of perfect agreement between the segmentations.

3.3   Search For Informative Spectral Bands

The workflow diagram provided in Figure 3-2 illustrates a process for selecting an informative spectral band from the HSI using the 3D RGA. The first step in the process is to choose a specific spectral band from HSI, which serves as a spectral address of a seed, for testing the band's ability to provide informative data about the area of interest. The selected spectral band is then subjected to the 3D RGA described in Section 3.1.

Once the algorithm completes its task, the segmented region is formed in the 3D space, as depicted in the Figure 3-2, where the segmented area is shown in red against the ground truth in white. The segmented 3D region is then mapped onto a two-dimensional plane. This step is done to compare the segmented region with the 2D ground truth of the datasets. The mapping creates a 2D binary mask by assigning a value of one to a pixel if the pixel is segmented across any of the spectral bands. This way the 3D segmented area is mirrored onto the spatial dimensions of the image.

The final stage of the process involves assessing the informativeness of the chosen spectral band based on the segmentation accuracy. This is quantified using two statistical measures: NMI and ARI. If both the NMI and ARI values exceed some threshold when comparing the segmented 2D region to the ground truth of the seed point, the spectral band is considered informative, indicating that it provides robust data for precise segmentation. As indicated in Figure 3-2, this threshold is set at 75%. However, for some classes, the NMI and ARI accuracy achieved across any spectral bands may be lower. In such cases, the threshold is adjusted to three-fourths of the maximum accuracy achieved across spectral bands. The three-fourths of maximum is chosen as a threshold to keep a balance between precision and generability. If these metrics do not meet the threshold, it implies that the spectral band is not informative enough, prompting another cycle of spectral band selection.
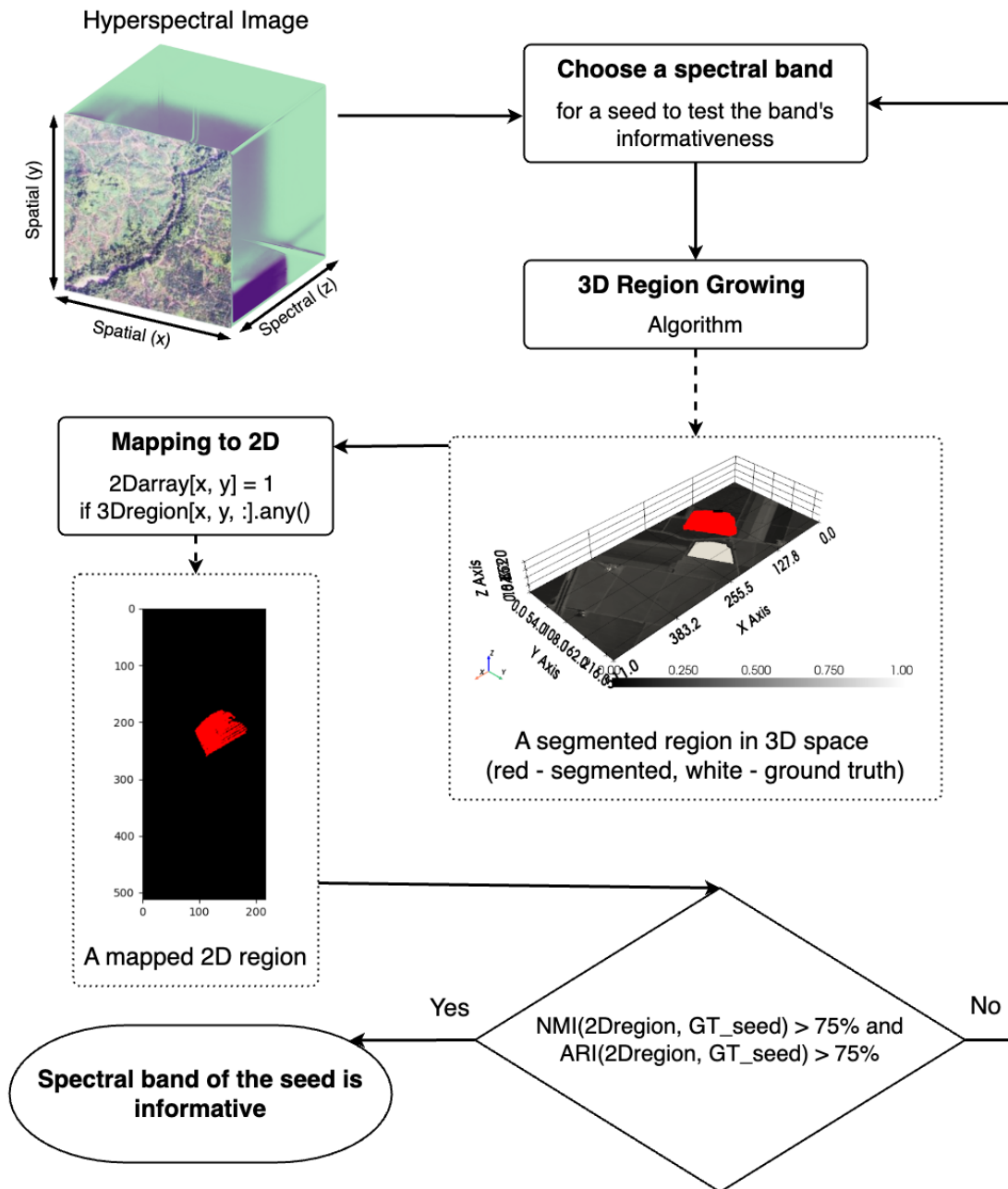
Figure 3-2: Workflow of spectral band selection process using 3D RGA.

Chapter 4

Experiments and Results

This chapter explain the experimental setup, presents the results and discusses them for each dataset employed. Each dataset provides a unique example, showcasing specific challenges and details that allow for a comprehensive evaluation of the effectiveness and adaptability of the proposed methodology. Finally, the proposed approach is compared with advanced methods to critically assess its performance relative to current methodologies in the field.

4.1 Experimental Setup

In this section, we detail the experimental framework, describing the datasets used, and how the final segmentation accuracy is achieved.

4.1.1 Datasets

Table 4.1 provides an overview of the datasets used in this sutdy. It includes key characteristics of each dataset, such as the sensor used to capture the HSI, the wavelength range and spectral resolution (in nanometers), spatial resolution (in meters), and the number of classes contained within each dataset. The Salinas, Indian Pines, and Pavia Centre datasets [106] are commonly employed for HSI segmentation tasks and have been selected to verify the performance of the methodology against their

ground truth. Meanwhile, the NERC-ARF dataset [107], an unlabeled dataset, is used to evaluate the methodology's applicability in real-world scenario.

Table 4.1: Summary of datasets

Dataset	Shape	Sensor	Range (nm)	Spectral res. (nm)	Spatial res. (m)	# of classes
Salinas	512x217x224	AVIRIS	400-2500	10	3.7	16
Indian Pines	145x145x224	AVIRIS	400-2500	10	20	16
Pavia Centre	1096x715x102	ROSIS	430-860	4	1.3	9
NERC-ARF	4759x8496x622	AisaFENIX	380-2500	3.5	30	NaN

Salinas Dataset

The Salinas scene, a 512 by 217 pixel image, was taken over the Salinas Valley in the USA in 1998 using the Airborne Visible InfraRed Imaging Spectrometer (AVIRIS) sensor [106]. Each pixel in this image represents a 3.7 square meter area. Initially, the image included 224 spectral bands, but 20 of these bands were later removed due to their redundancy. Specifically, bands associated with water absorption ([104–108], [150–163], and 220) were excluded. The refined image comprises 16 classes that include various stages of crops and vegetation, such as two types of Broccoli green weeds, different states of Fallow land, Stubble, Celery, Grapes (both untrained and in different development stages), Corn with senesced green weeds, Lettuce romaine at four growth stages (4, 5, 6, and 7 weeks), and Vineyards (both untrained and with a vertical trellis).

Indian Pines Dataset

The Indian Pines dataset, captured by the AVIRIS sensor over the Indian Pines test site in North-western Indiana, USA in June 1992, consists of 224 spectral reflectance bands [106]. After excluding bands associated with water absorption, 204 bands within the 400 to 2500 nanometer wavelength range were retained. In the Indian Pines area, agricultural land accounts for two-thirds of the terrain, while the rest is covered by forests and various types of natural vegetation. The region is characterized

by two significant dual-lane highways, a railroad track, and includes areas of sparse residential buildings, additional man-made structures, and lesser thoroughfares. Captured during June, the image displays early growth phases of specific crops, such as corn and soybeans, which occupy less than 5% of the land. The ground truth data is divided into sixteen categories, which contains mixed categories.

Pavia Centre Dataset

The Pavia Centre scene was captured using the Reflective Optics System Imaging Spectrometer (ROSIS) sensor during an aerial survey above Pavia in northern Italy in 2002 [106]. The sensor collected hyperspectral data in the 430-860 nanometer range of the visible and infrared spectrum, achieving a spatial resolution of 1.3 meters. It represents the urban landscape of Pavia's city center, characterized by densely packed buildings, open spaces, and the Ticino river. Spatially, the width and height of the image are 1096 and 715, respectively. Spectrally, it contains 102 bands. The ground truth for the image identifies nine distinct classes. It includes materials such as bricks, water, asphalt, bitumen, soil, tiles, among others.

NERC-ARF Dataset

The Natural Environment Research Council Airborne Research Facility (NERC-ARF) supplied numerous HSI datasets from the Danum Valley in Malaysia, utilizing the Specim Aisa FENIX imager [107]. The specific dataset used in this study is designated with the code "2014_288 - RG13_06 Flight," captured on 15 October 2014. Currently, this dataset lacks ground truth. Among the sensors evaluated in this study, the Aisa Fenix offers the widest spectral range, spanning from 380 to 2500 nanometer, resulting in a total of 622 bands. To mitigate computational complexity, the spectral bands were lowered to 207 through a resampling process that averages the data within non-overlapping, fixed bins, each comprising three bands.

In addition to the spectral downsampling, the spatial dimensions were also reduced. Initially, the image was rotated by 20 degrees to correct for the aircraft flight's specifications, which caused the image lines to appear diagonal, as illustrated

in Figure 4-1 (a). Subsequently, the image was cropped into ten smaller regions, each with dimensions of 848 by 475 pixels. Only one of these regions, depicted in Figure 4-1 (b), was utilized for further analysis.
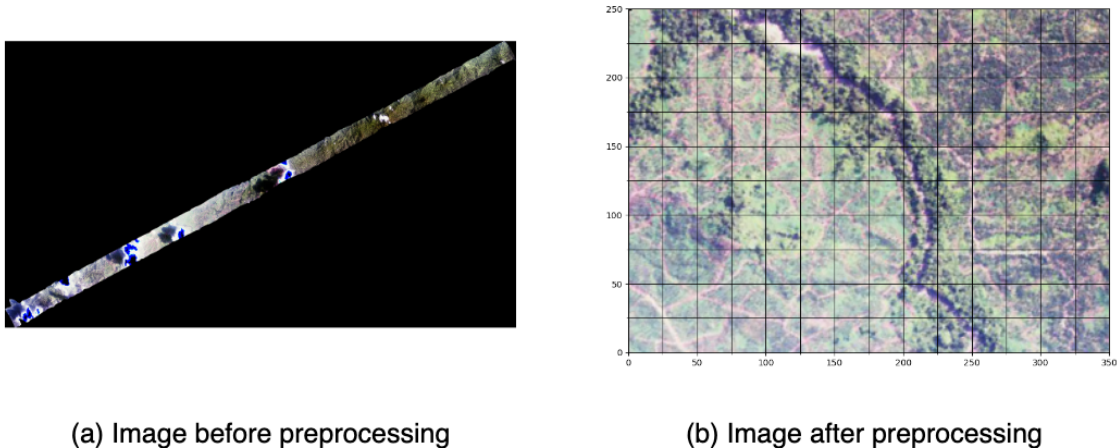
(a) Image before preprocessing   (b) Image after preprocessing

Figure 4-1: NERC-ARF dataset.

4.1.2 Final Segmentation Process

During the experiments, it was observed that there typically is not just a single informative spectral band but rather a range of them. This phenomenon can be attributed to the high correlation among adjacent spectral bands. Consequently, final segmentation accuracy is achieved by averaging the results across this informative spectral range. This step is crucial for comparing the performance of the current methodology with other state-of-the-art (SOTA) methods.

The initial step in averaging results across the spectral range involves selecting ten equidistant spectral bands in the informative range corresponding to the class under study. The number of bands is chosen to be ten as a good balance between covering the entire spectral range of interest and maintaining a manageable dataset size. Then, ten seeds, representing these ten spectral bands, initiate ten 3D regions that are later mapped to a 2D space, as discussed in Section 3.3. Two methods are employed to aggregate segmentation results across ten regions. In the first method, a pixel is marked as segmented in the 2D array if it is included in the segmentation results of

all ten regions (named as "All-regions consensus" method). In the second method, a pixel is marked if it appears in the segmentation results of at least five regions (named as "Majority-regions rule" method). This approach allows for smoothing the results across ten regions. To evaluate the segmentation result, the final aggregated region is compared with the class of the seed point, and accuracy is quantified by MNI and ARI scores.

4.2   Salinas Dataset
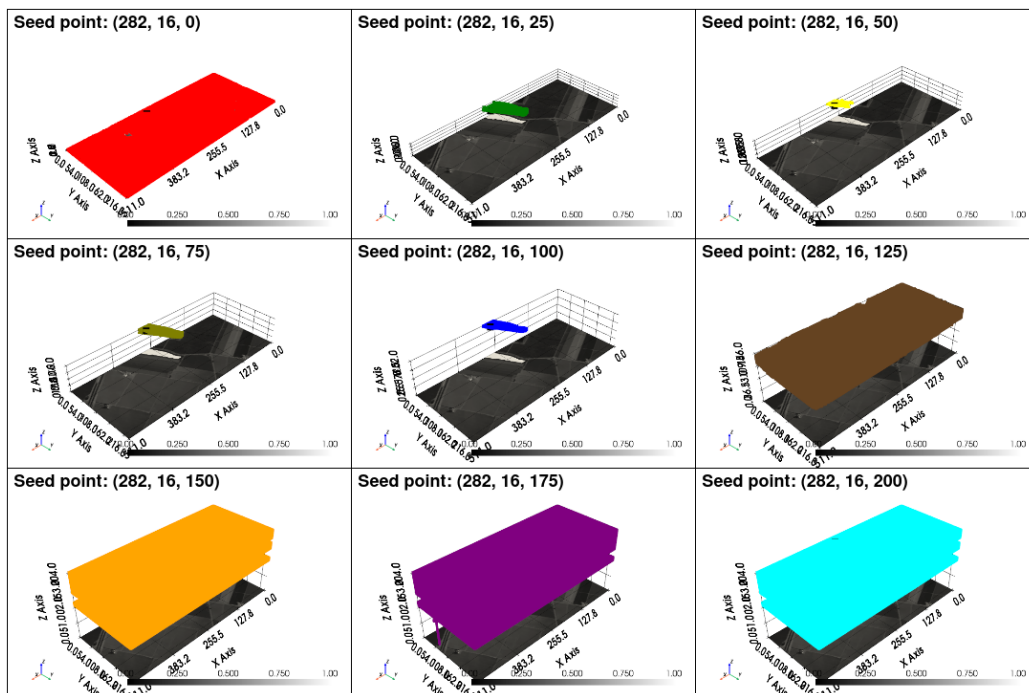
Figure 4-2: 3D segments of Salinas dataset across various spectral bands.

Figure 4-2 provides a visual representation of the selection process for informative spectral bands using the 3D RGA. This figure displays nine segmented regions generated by the 3D RGA using seed points across various spectral bands, specifically at every 25th band interval. The seed point is selected from "broccoli_green_weeds_1" class within the Salinas dataset and its spatial position is the same across segmentations. Each sub-figure presents a gray-scale image of Salinas, a colored segmented region, and ground truth of the class highlighted in white. From this figure, it is

evident that the segmented regions with seeds at spectral bands 25, 50, 75, and 100 closely correspond to the actual class. This matching behavior is observed across spectral bands from 20 to 100. In contrast, for the other bands, the segmented regions cover the entire image, indicating an absence of class differentiation.

Table 4.3 offers a detailed overview of the segmentation results for the Salinas dataset, achieved by using the most informative spectral bands. This analysis comprises of sixteen distinct classes that represent various types of vegetation. The "Bands" column specifies the range of spectral bands identified as most informative for segmenting each particular class through our methodology. The "Wavelength" column provides the range of wavelengths (in nanometers) corresponding to the selected bands. As datasets, with the exception of NERC-ARF, do not specify the wavelength associated with each spectral band, the approximate wavelength is calculated based on each dataset sensor's wavelength range and its spectral resolution. Additionally, this table presents the final NMI and ARI segmentation accuracy metrics for each class, employing two distinct aggregation strategies: the All-Regions Consensus (ARC) and the Majority-Regions Rule (MRR).

Table 4.3: Segmentation results for Salinas dataset using most informative bands

#	Class	Bands	Wavelength	All-regions consensus		Majority-regions rule	
				NMI ↑	ARI ↑	NMI ↑	ARI ↑
1	broccoli_green_weeds_1	20-100	578-1328	0.5904	0.7462	0.791	0.879
2	**broccoli_green_weeds_2**	20-35	578-719	**0.8436**	**0.9272**	0.8442	0.9198
3	Fallow	20-30	578-672	0.5465	0.7182	0.5818	0.733
4	Fallow_rough_plow	40-60	766-953	0.664	0.7972	0.7438	0.8397
5	Fallow_smooth	10-70	484-1047	0.8094	0.9038	0.791	0.8865
6	Stubble	15-35	531-719	0.758	0.881	0.7202	0.8539
7	Celery	10-40	484-766	0.7916	0.8994	0.8279	0.9101
8	Grapes_untrained	60-80	953-1141	0.4473	0.5905	0.4598	0.6007
9	Soil_vinyard_develop	40-60	766-953	0.781	0.892	0.8819	0.9484
10	Corn_senesced_green_weeds	40-60	766-953	0.3436	0.4524	0.7508	0.8652
11	Lettuce_romaine_4wk	10-70	484-1047	0.6441	0.774	0.7667	0.8745
12	Lettuce_romaine_5wk	40-70	766-1047	0.433	0.5928	0.7904	0.8775
13	Lettuce_romaine_6wk	35-60	719-953	0.5552	0.6709	0.7094	0.8245
14	Lettuce_romaine_7wk	25-35	625-719	0.5086	0.6684	0.4917	0.6404
15	**Vinyard_untrained**	65-85	1000-1188	0.6107	0.7403	**0.9045**	**0.9632**
16	Vinyard_vertical_trellis	5-35	438-719	0.7437	0.864	0.7929	0.8809
Average:				0.6537	0.7899	**0.7463**	**0.8542**
Joining all classes:				0.5763	0.4417	0.7719	0.706
SOTA [108]:						0.91	0.85

Moreover, Table 4.3 presents average scores across classes, the scores obtained by joining all classes, and the SOTA results from [108] to facilitate the comparison. The inclusion of the accuracy for the joined classes addresses a gap in the literature, where typically only the accuracy of whole scene mapping is reported. For example, Figure 4-3 presents a visual comparison between the ground truth of the Salinas dataset and our joined segmentation result. The joined result is achieved by first performing a separate segmentation for each class, followed by merging these individual segments into a single image. This figure demonstrates that a relatively simple algorithm, such as the 3D RGA, can yield comparable results when applied to carefully chosen spectral bands.
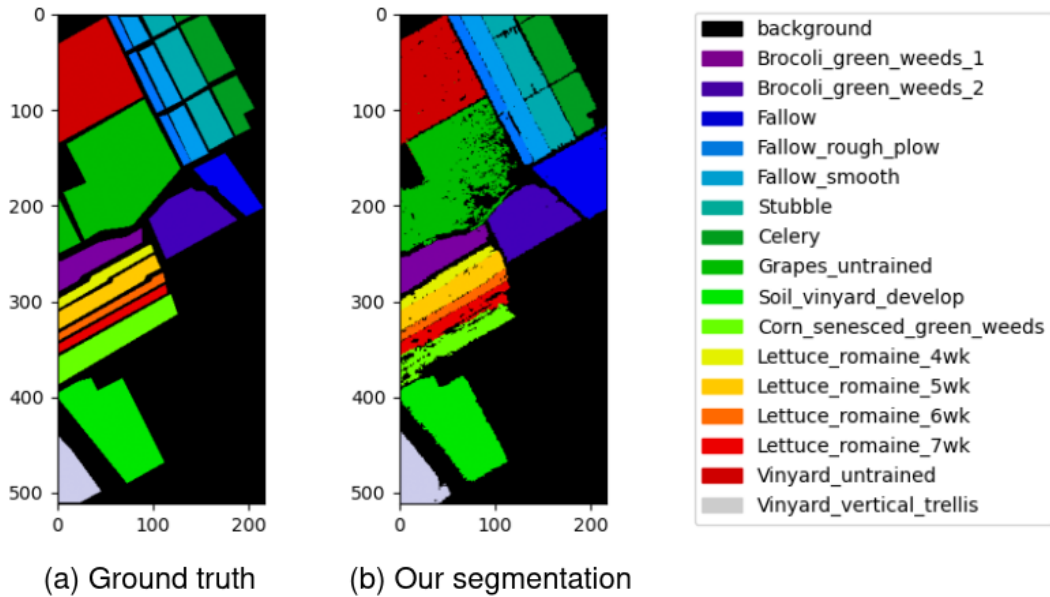
Figure 4-3: Segmentation results and ground truth of Salinas dataset

One point to note is that classes 4-8 (namely, "Fallow_rough_plow", "Fallow_ smooth", "Stubble", "Celery", "Grapes_untrained") consisted of two or three disconnected regions. Consequently, separate seed points from each sub-region were selected, and segments from these sub-regions were combined to obtain a final result for each class.

It should be noted that even though some classes fall under a single vegetation group, they exhibit differences in their informative spectral bands. For instance,

"broccoli_green_weeds_1" is segmented within the wavelength range of 578-1328 nanometers, achieving NMI of 0.791 and ARI of 0.879. The second type of Broccoli green weeds is segmented within a narrower wavelength range of 578-719 nanometers, achieving NMI of 0.8442 and ARI of 0.9198. However, when the first type is segmented using the same spectral ranges as the second, both NMI and ARI scores decrease. A similar pattern is observed for different types of Lettuce romaine. This observation underscores the importance of selecting appropriate spectral bands for segmentation within vegetation groups, as different classes, even within the same group, have unique spectral characteristics.

Referring to Figure 1-1, another noteworthy observation is that the wavelength range for most of the classes begins in the spectrum corresponding to green color (starts from 520 nanometer), with the exception of "Vineyard_vertical_trellis" class. "Broccoli_green_weeds_1" is the only class that extends into the middle infrared spectrum, whereas the others are primarily within the near infrared, with a few limited to the visible light spectrum ("broccoli_green_weeds_2", "Stubble", "Lettuce_romaine_7wk", "Vinyard_vertical_trellis"). This analysis highlights the diversity in spectral range usage among different vegetation classes.

Results across the classes showed variability in both NMI and ARI scores, reflecting differences in the segmentation performance related to the characteristics of each class and the selected spectral bands. For instance, classes such as "broccoli_green_weeds_2" and "Vinyard_untrained" demonstrated high segmentation accuracy, as evidenced by their respective NMI and ARI scores, particularly under the MRR averaging strategy. Conversely, some classes, such as "Corn_senesced _green_weeds," exhibited lower performance, underscoring the challenges in segmenting certain vegetation types.

The MRR generally outperforms the ARC strategy, as evidenced by higher average NMI and ARI scores (0.7463 and 0.8542, respectively, compared to 0.6537 and 0.7899). Specific classes, such as "Vinyard_untrained" and "Corn_senesced_green_weeds," demonstrate substantial improvement under the MRR compared to the ARC. It may be due to the fact that ARC is equivalent to the AND logical operation across ten

regions, thus, it reflects the smallest region. Segmentation in certain bands often led to small regions, even though being in the informative band range (for example, the third sub-figure in Figure 4-2), probably due to noise in spectral reflectance data. Additionally, seed points located at the edges typically resulted in smaller than ground truth regions compared to those in the center. Therefore, focusing on the majority regions within each class led to a more accurate segmentation outcome.

While the average performance under the MRR approach shows competitive results (NMI: 0.7463, ARI: 0.8542), it falls short of the SOTA benchmark (NMI: 0.91, ARI: 0.85) in terms of NMI. Yet it surpasses in ARI, indicating areas for potential improvement and the effectiveness of this approach in certain contexts. However, when we join all classes as one segmentation result, the SOTA performs better both on NMI (0.91 compared to 0.7719) and ARI (0.85 vs. 0.706). It can explained by the fact that the methodology is not devised to the whole scene mapping but to identify a single region.

4.3   Indian Pines Dataset

Table 4.5 provides an overview of segmentation results obtained for the Indian Pines dataset through the usage of the most informative spectral bands. Table's structure is the same as for the Salinas dataset. The analysis comprises of sixteen distinct classes that represent various classes of vegetation and man-made structures.

Identifying informative spectral bands for the Indian Pines dataset presented challenges for two primary reasons. First, the majority of the classes, with the exception of classes "Alfalfa", "Corn", "Grass-pasture-mowed", "Hay-windrowed", "Oats", "Wheat", and "Stone-Steel-Towers", were composed of multiple smaller subregions. True classes can be seen from Figure 4-4. These smaller areas proved difficult to accurately analyze, likely due to distortion from adjacent pixels. Additionally, these subregions showed preferences for different spectral ranges, even within the same class, complicating the task of identifying a single spectral range suitable for the entire class. For instance, in the case of "Soybean-clean", distinct subregions showed

Table 4.5: Segmentation results for Indian Pines dataset using most informative bands

#	Class	Bands	Wavelength	All-regions consensus		Majority-regions rule	
				NMI	ARI	NMI	ARI
1	Alfalfa	35-45	719-813	0.781	0.8678	0.0081	0.0054
2	Corn-notill	25-45	625-813	0.062	0.1776	0.0032	-0.0109
3	Corn-mintill	55-57	906-925	0.3256	0.4687	0.0187	-0.043
4	Corn	22-36	597-728	0.2401	0.2959	0.3509	0.4293
5	Grass-pasture	20-70	578-1047	0.2832	0.4747	0.0082	-0.0292
6	Grass-trees	30-40	672-766	0.179	0.2491	0.0508	-0.0077
7	Grass-pasture-mowed	35-45	719-813	0.7322	0.8247	0.0022	-0.0006
8	Hay-windrowed	118-138	1544-1731	0.5958	0.7118	0.2303	0.2848
9	Oats	30-50	672-859	0.5042	0.6308	0.0022	0.0004
10	Soybean-notill	39-49	756-850	0.1702	0.3538	0.0493	-0.0309
11	Soybean-mintill	30-40	672-766	0.3007	0.5028	0.0002	-0.0019
12	Soybean-clean	10-50	484-859	0.431	0.5709	0.0088	-0.025
13	**Wheat**	35-39	719-756	**0.8108**	**0.9015**	**0.8764**	**0.9412**
14	Woods	25-35	625-719	0.3712	0.5677	0.2616	0.2972
15	Buildings-Grass-Trees-Drives	20-25	578-625	0.6086	0.7516	0.5738	0.7115
16	Stone-Steel-Towers	2-25	409-625	0.722	0.835	0.755	0.8583
	Average:			**0.4841**	**0.6233**	0.1981	0.1549
	Joining all classes:			0.4069	0.3347	0.2676	0.0068
	SOTA [109]:			0.517	0.283		

optimal performance with different sets of spectral bands: (13-17, 38-50) for one, (23-35, 40-62) for another, and (10-28) for a third. Secondly, the presence of mixed classes within the Indian Pines dataset indicates that the spectral signatures do not exclusively represent a single category, further complicating the segmentation process. It is especially the case for classes such as "Grass-trees", "Grass-pasture", "Woods".

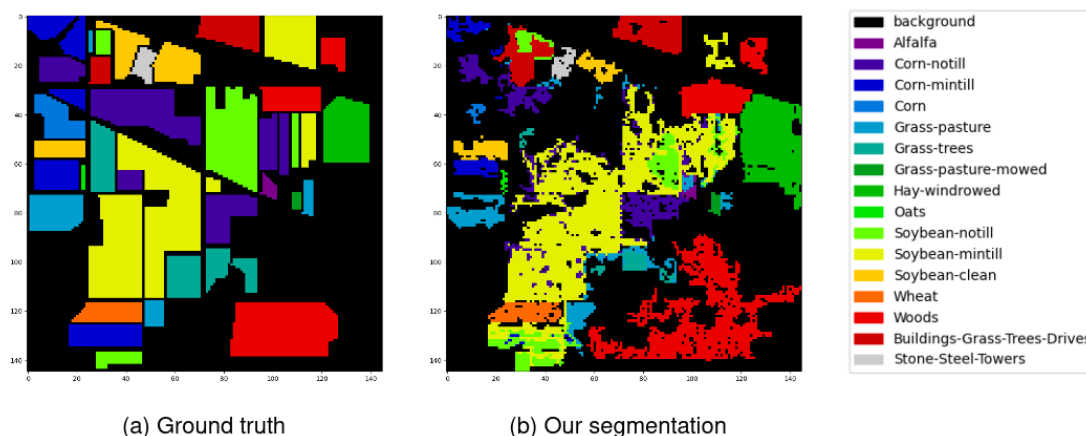(a) Ground truth   (b) Our segmentation

Figure 4-4: Segmentation results and ground truth of Indian Pines dataset

The Indian Pines image has a lower spatial resolution (20 meters per pixel) com-

pared to the Salinas (3.7 meters per pixel), meaning each pixel in the Indian Pines dataset covers a larger area on the ground than each pixel in the Salinas dataset. Lower resolution means less detail and can lead to a greater challenge in identifying small land cover patches, which also may explain lower segmentation accuracy than for Salinas on all metrics. It also can be a reason for the Indian Pines' significantly poorer performance using the MRR method in comparison to ARC.

Another critical observation from the table is the variability in segmentation effectiveness across different classes and aggregation methods, similar to Salinas' results. For instance, the "Wheat" class shows remarkably high scores under both averaging strategies, with NMI and ARI reaching up to 0.8108 and 0.9015, respectively, under ARC, and even higher under MRR. Conversely, classes like "Corn-notill" and "Soybean-notill" exhibit significantly lower effectiveness, with negative ARI scores under the MRR, indicating a lack of consensus between segmentation results and ground truth.

The average scores across all classes are moderate, with an NMI of 0.4841 and an ARI of 0.6233 under ARC, dropping significantly under the MRR. When joining all classes, the effectiveness decreases further, especially notable in the ARI under the MRR, decreasing to 0.0068. However, ARI scores under ARC surpasses the SOTA benchmark score of 0.283 [109] demonstrating potential for improvement.

4.4 Pavia Centre Dataset

Table 4.7 provides a comprehensive overview of segmentation results obtained for the Pavia Centre dataset through the usage of the most informative spectral bands. The analysis comprises of nine distinct classes that represent various classes of urban and natural landscapes.

The SOTA benchmark [108] for NMI and ARI significantly surpasses the results achieved in this study. Similar to the Indian Pines dataset, all classes in the Pavia Centre, except for "Water," consist of small, disjoint subregions. Figure 4-5 shows ground truth of "Trees", "Tiles", and "Meadows" classes highlighted in white. Despite

Table 4.7: Segmentation results for Pavia Centre dataset using most informative bands

#	Class	Bands	Wavelength	All-regions consensus		Majority-regions rule	
				NMI	ARI	NMI	ARI
1	**Water**	4-102	443-856	**0.7294**	**0.8451**	**0.4854**	**0.5874**
2	Trees	0-70	430-721	0.0532	0.1433	0.0307	0.0768
3	Asphalt	25-50	531-637	0.1139	0.2328	0.0635	0.1256
4	Self-Blocking Bricks	35-75	573-742	0.2424	0.3966	0.2966	0.4699
5	Bitumen	52-102	645-856	0.1846	0.3057	0.2286	0.4106
6	Tiles	8-48	460-628	0.076	0.1535	0.0483	0.0914
7	Shadows	82-102	772-856	0.4312	0.6046	0.397	0.5937
8	Meadows	0-45	430-616	0.015	0.0222	0.0725	0.139
9	Bare Soil	0-80	430-763	0.0434	0.1217	0.0434	0.1217
Average:				**0.2099**	**0.3139**	0.1851	0.2907
SOTA [108]:				0.91	0.97		

the high spatial resolution of Pavia Centre (1.3 meters), the subregions are too small for meaningful segmentation, probably due to interference from pixels of neighbouring classes. Furthermore, the high number of subregions makes it even more challenging to select seed points from each subregion.

(a) "Tiles" class   (b) "Trees" class   (c) "Meadows" class
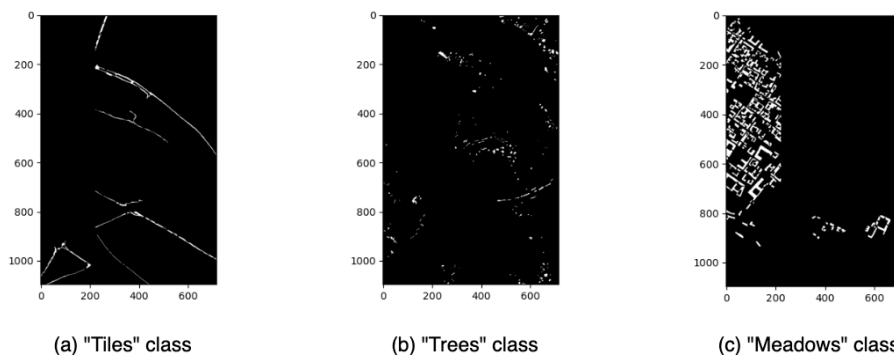
Figure 4-5: Ground truth of Pavia Dataset.

Certain classes that are more uniform, such as "Water" and "Self-Blocking Bricks", showed relatively high segmentation effectiveness, with NMI and ARI scores indicating a strong agreement between the segmentation results and the ground truth. On the other hand, classes such as "Trees" and "Meadows" with many disjoint subregions exhibited low NMI and ARI scores, highlighting the challenges in accurately segmenting these classes. Thus, it can be concluded that the proposed methodology's

44

limitation lies in its reliance on datasets featuring larger, more homogeneous regions.

Another potential reason for the poor accuracy observed with the Pavia Centre is the wavelength range it captures, which is almost 5 times narrower than that of other datasets used in this study. It primarily captures visible light and a small portion of near-infrared light (430-860 nanometers). 10 out of the 16 classes in the Salinas dataset and 3 out of the 16 in the Indian Pines dataset contain spectral information beyond 860 nanometers. Therefore, it can be suggested that some critical information might be contained in wavelengths beyond what the Pavia Centre captures.

4.5 NERC-ARF Dataset

As the NERC-ARF dataset does not have ground truth, analysis required additional steps. Spatial positions of 140 seed points were chosen at the intersection of the grids in Figure 4-1 (b). Every third band was chosen as spectral position for the every spatial positions of the seed. After running the 3D RGA for each arranged seed point, we obtained 9800 binary mask arrays of segmentation. These images were further clustered using Mean-Shift Clustering (MSC).

MSC is widely used in tasks related to computer vision, such as image segmentation, to classify pixels into regions according to their color and proximity in space [110]. This process includes placing a kernel on every data point, finding the average of points within the kernel, and moving the kernel toward the average point. The approach is iterative and does not require any prior information about the number of clusters, as the algorithm can determine the number of clusters based on the data.

MSC initially produced 21 segmentation clusters. After merging similar clusters, the total was reduced to 18. Figure 4-6 displays representative images from each cluster, with segmented regions shown in white. For instance, Cluster 1 features segmentation across the entire image, whereas Cluster 18 has a segmented region so small it is barely noticeable, containing only 31 pixels out of 87500 at maximum. In Clusters 3, 4, and 5, all areas except for rivers are segmented. The segmentation outcome

45

also varies depending on the seed point's location relative to the river; specifically, whether it's on the river's right or left side. For example, in Clusters 8 and 16, the segmentation extends across the entire region up to the river.
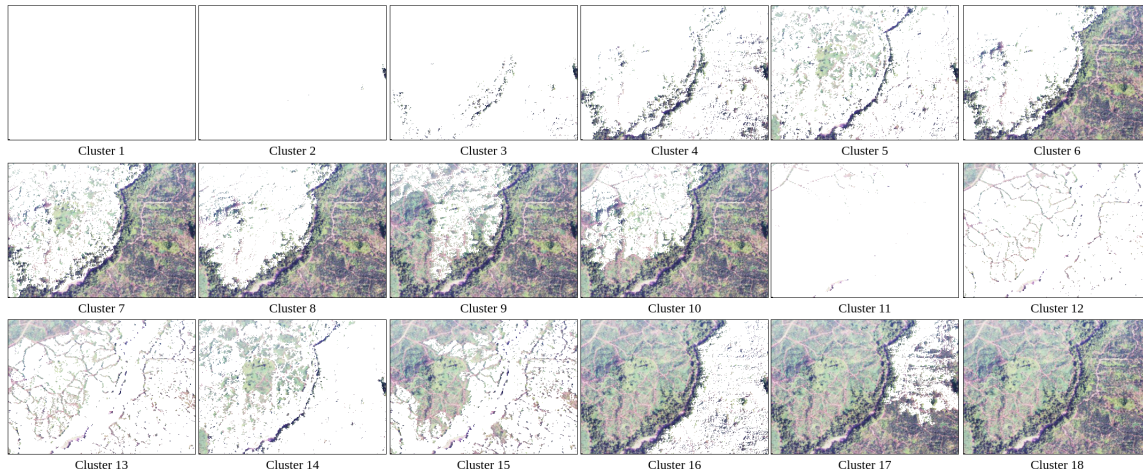

Figure 4-6: Clusters obtained for NERC-ARF dataset.

Table 4.9: Segmentation results for NERC-ARF dataset

Bands	Segmentation results	Comments
0-14	Cluster 1	No unique information, whole image segmented
15-29	Clusters 1, 2, 3, 4, 6, 8, 11	
30-39	Clusters 1, 2, 3, 4, 6, 8, 9, 11, 12, 16, 17	Contains some local regions
40-64	Clusters 1, 2, 3, 4, 8, 11, 12, 13, 15	Contains some local regions
65-104	Cluster 18	Regions are too small to be visible, the largest region contains 31 pixels out of 87500
105-114	Clusters 4, 5, 6, 7, 8, 10, 14, 15, 16, 17	Contains some local regions
115-139	Clusters 1, 14, 18	Rich for local regions
140-149	Cluster 1	No unique information, whole image segmented
150-164	Clusters 1, 3, 4, 6, 8, 16	Contains some local regions
165-207	Cluster 1	No unique information, whole image segmented

An examination of how clusters are distributed across spectral bands has led to some insights regarding the informativeness of these bands. Table 4.9 presents a summary of these findings. Bands ranging from 0-14, 140-149, and 165-207 are deemed uninformative, as segmentation across the entire image in these bands suggests a lack of unique information. Conversely, bands 65-104 exclusively contain Cluster 18, indicating information that may not be generalizable. Bands 30-39, 40-64, and 105-114 show the most diversified segmentation, suggesting they could potentially contain

useful information. Furthermore, bands 115-139 reveal interesting results, featuring local regions that, while not as small as those in Cluster 18, are smaller than those in other clusters. Figure 4-7 shows examples of some of those regions at bands 115-139. This pattern might imply that these bands capture specific features with a localized impact, distinct enough to be segmented.
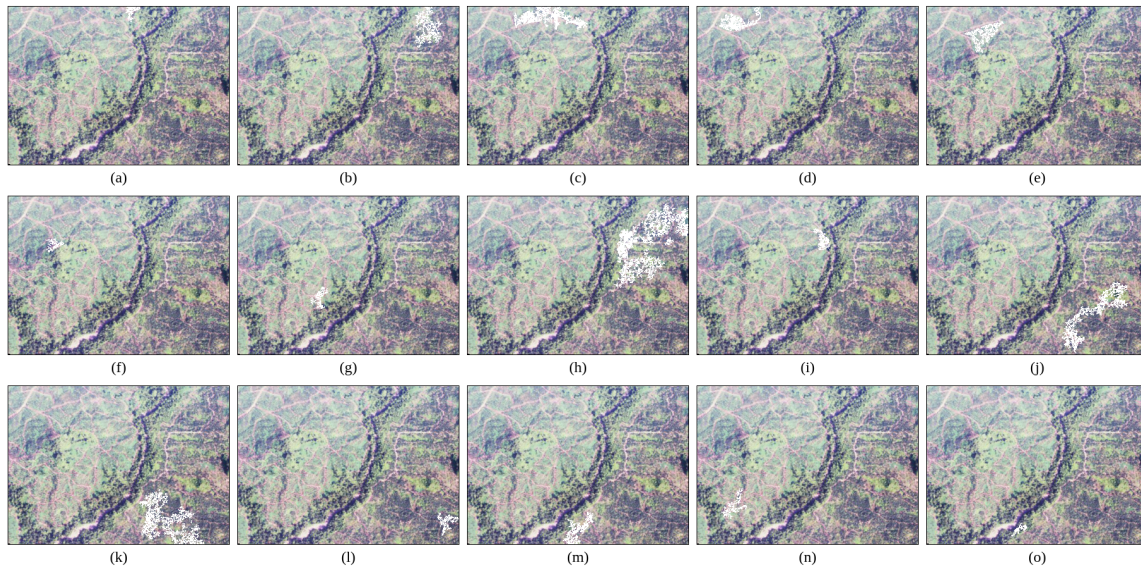

Figure 4-7: Local regions obtained at bands 115-139 for NERC-ARF dataset.

4.6 Comparison With State-Of-The-Arts

To evaluate if selected bands enhance segmentation outcomes compared to other dimensionality reduction techniques, segmentation of the Salinas image using MSC is conducted. Each execution of MSC starts with a randomly chosen initial mean, causing variability in the final outcomes. To obtain stable NMI and ARI scores, 10 trials are conducted. Although the seed of the random function varies across trials, it remains consistent within each experiment.

For these experiments, MSC is applied to the original image, to spectral features extracted by PCA and CAE, and to spectral bands selected within the range proposed by the method. PCA is carried out using a function from the Spectral library in Python [111]. For the CAE, 1D convolutions are employed to reduce the spectral

47

dimension only, as outlined in prior work [112]. The architecture of the 1D CAE comprises an encoder-decoder network, each featuring four convolutional layers followed by max pooling and leaky ReLU activations. Regarding the selected bands, the minimum and maximum bands determined for the Salinas dataset are utilized, thus reducing the image to bands 5-100.

Table 4.11 summarizes the experimental results using the NMI score. On average, NMI accuracy stands at 47.27% with original image. This accuracy decreases by 13% with the use of CAE. The scores slightly improve by 0.07% with the selected bands, though the improvement is more notable with PCA, at 0.13%.

Table 4.11: NMI of segmentation with different dimensionality reduction methods

	NMI score	The difference from NMI of original image		
trial	Original image	PCA-reduced image	CAE-reduced image	Bands [5-100]
1	42.24%	**1.53%**	-8.50%	**1.64%**
2	48.63%	**0.24%**	-15.31%	**1.11%**
3	43.63%	**0.25%**	-8.58%	-0.57%
4	49.22%	-0.07%	-15.51%	**0.11%**
5	51.75%	**0.31%**	-17.49%	-0.50%
6	51.46%	**0.16%**	-15.85%	**0.05%**
7	41.71%	**0.65%**	-9.05%	-0.04%
8	43.10%	-1.02%	-8.27%	-1.60%
9	49.09%	-0.23%	-16.09%	**0.86%**
10	51.88%	-0.50%	-16.08%	-0.37%
Average:	47.27%	**0.13%**	-13.07%	**0.07%**

Similarly, Table 4.12 presents ARI scores for the same experiments. When using images reduced by CAE, the clustering results decrease by 18.75%. For PCA, there is an improvement of 0.54%, while the use of selected bands results in an even better improvement of 0.98%.

The experiments demonstrate the importance of choosing the right dimensionality reduction technique. While CAE is a powerful tool for feature extraction and dimensionality reduction in many contexts, its application here suggests that not all information critical for segmentation is retained through its process. On the other hand, simpler methods like PCA or even manual selection of bands based on the proposed method can provide better segmentation outcomes.

48

Table 4.12: ARI of segmentation with different dimensionality reduction methods

| | ARI score | The difference from ARI of original image | | |
trial	Original image	PCA-reduced image	CAE-reduced image	Bands [5-100]
1	10.57%	**1.17%**	-4.43%	**7.37%**
2	40.45%	**0.53%**	-28.63%	**0.33%**
3	9.95%	**4.25%**	-0.15%	**6.68%**
4	40.61%	-0.09%	-29.40%	-0.22%
5	39.55%	-0.11%	-32.53%	-0.69%
6	39.67%	-0.27%	-30.53%	-0.20%
7	10.92%	**0.93%**	**0.57%**	-0.13%
8	11.45%	-0.67%	-2.92%	-2.81%
9	40.81%	-0.44%	-29.52%	-0.40%
10	39.63%	**0.14%**	-29.93%	-0.16%
Average:	28.36%	**0.54%**	-18.75%	**0.98%**

4.7 Depth Analysis

(a) Seed (298, 10, 31) covers bands (17, 37)   (b) Seed (285, 39, 96) covers band (96)
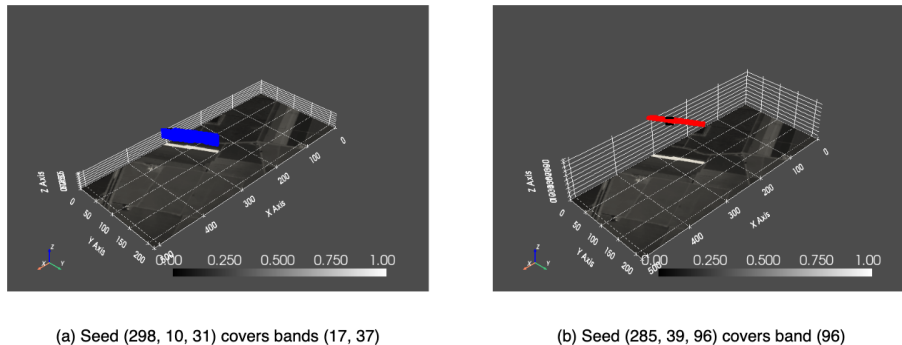
Figure 4-8: Depth of 3D segmented regions from Salinas dataset.

The process of projecting a segmented region from 3D space to a 2D array is achieved through a simple mirroring technique. However, examining the shape of the 3D regions suggests that the depth of these regions may also convey important information. For instance, as illustrated in Figure 4-8, two seed points located in different spectral bands but within the same class in the Salinas dataset can result in regions with significantly different depths: one with a depth of 20 (a) and another with a depth of 1 (b). Seeds originate from the "Lettuce_romaine_4wk" class, and thus, their informative bands fall within the range of 10-70. Consequently, a region that begins from a seed point within the spectral band of 31 leads to a deeper region compared to a seed with a spectral address outside of this class's informative bands.

Additionally, a heatmap has been constructed for the NERC-ARF dataset, where

each pixel represents the frequency of segmented spectral bands. Figure 4-9 illustrates that pink areas in the original image are segmented more frequently than other regions, with approximately 20 or more out of 207 spectral bands corresponding to these areas. It may suggest that the pink areas likely have a distinctive spectral signature that makes them stand out from the rest of the landscape. This distinctiveness could be due to specific characteristics of the surface that reflect light differently compared to surrounding areas. Therefore, future work could consider examining the impact of depth and developing an improved 3D-to-2D mapping procedure.
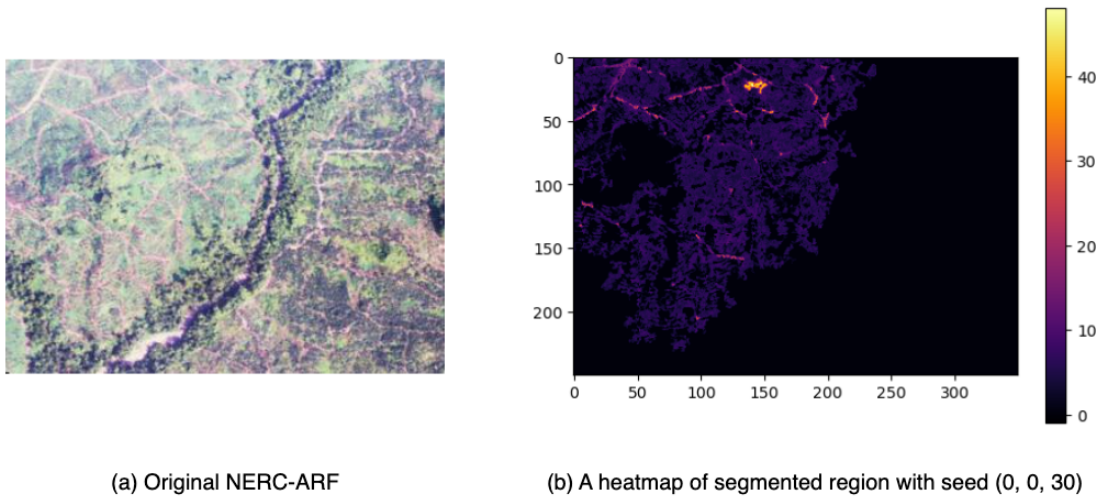

(a) Original NERC-ARF   (b) A heatmap of segmented region with seed (0, 0, 30)

Figure 4-9: Depth of a 3D segmented region in NERC-ARF dataset.

Chapter 5

Conclusion

The thesis introduced a novel method that employs a 3D RGA for the effective band selection, with the goal of enhancing segmentation accuracy in HSI data. Unlike conventional band selection methods that focus on statistically distinct bands, this approach utilizes a heuristic search for the most informative bands, considering both spatial and spectral information. Furthermore, the method's unique stopping criterion, based on the intensity of the seed pixel, enables flexible and precise control over the segmentation process.

Our experiments across various datasets, including Salinas, Indian Pines, Pavia Centre, and NERC-ARF, showcased the capability of our approach in achieving competitive segmentation accuracy. The experiments indicated that, typically, there is not just one informative spectral band; instead, a range of bands was identified as significant. The segmentation accuracy, assessed using NMI and ARI, varied across different classes within the same dataset, highlighting differences in spectral characteristics of each region. Moreover, we noted variations in informative wavelength ranges, classes covering different segments of electromagnetic spectrum. Additionally, it was observed that even within the similar vegetation groups, classes could have differing informative spectral bands. Our methodology proved useful in analyzing unlabeled HSI datasets, as evidenced by the results with the NERC-ARF dataset.

However, the methodology has limitations, particularly as its performance decreases in cases where a class is composed of disjointed, small regions. This condition

complicates the selection of seeds for each region and may introduce noise due to spectral signatures being disrupted by surrounding pixels. Additionally, the method's effectiveness depends on the spatial and spectral resolution of the captured image, with higher resolutions being preferable. Finally, integrating separate regions into a single image led to performance that fell below the SOTA across all datasets. This outcome likely stems from the method not being intended for scene segmentation.

By comparing our method against SOTA approaches, it became clear that while there are areas for improvement — particularly in handling datasets with smaller, less homogeneous regions — our methodology still offers a competitive advantage in certain situations. Therefore, future work could aim to refine the methodology further by automating the selection of seed points to better manage small, disjointed regions. Additionally, future research could explore assessing the impact of depth in 3D regions and developing an improved procedure for mapping from 3D to 2D.

Bibliography

[1] Pramod K Varshney, Manoj K Arora, Richard Lucas, Aled Rowlands, Olaf Niemann, and Ray Merton. Hyperspectral sensors and applications. *Advanced image processing techniques for remotely sensed hyperspectral data*, pages 11–49, 2004.

[2] Muhammad Jaleed Khan, Hamid Saeed Khan, Adeel Yousaf, Khurram Khurshid, and Asad Abbas. Modern trends in hyperspectral image analysis: A review. *Ieee Access*, 6:14118–14129, 2018.

[3] Atiya Khan, Amol D Vibhute, Shankar Mali, and CH Patil. A systematic review on hyperspectral imaging technology with a machine and deep learning methodology for agricultural applications. *Ecological Informatics*, 69:101678, 2022.

[4] Dhritiman Saha and Annamalai Manickavasagan. Machine learning techniques for analysis of hyperspectral images to determine quality of food products: A review. *Current Research in Food Science*, 4:28–44, 2021.

[5] Natsuo Okada, Yohei Maekawa, Narihiro Owada, Kazutoshi Haga, Atsushi Shibayama, and Youhei Kawamura. Automated identification of mineral types and grain size using hyperspectral imaging and deep learning for mineral processing. *Minerals*, 10(9):809, 2020.

[6] Baowei Fei. Hyperspectral imaging in medical applications. In *Data Handling in Science and Technology*, volume 32, pages 523–565. Elsevier, 2019.

[7] Costanza Cucci and Andrea Casini. Hyperspectral imaging for artworks investigation. In *Data handling in science and technology*, volume 32, pages 583–604. Elsevier, 2019.

[8] Alberto Signoroni, Mattia Savardi, Annalisa Baronio, and Sergio Benini. Deep learning meets hyperspectral image analysis: A multidisciplinary review. *Journal of Imaging*, 5(5):52, 2019.

[9] Reaya Grewal, Singara Singh Kasana, and Geeta Kasana. Machine learning and deep learning techniques for spectral spatial classification of hyperspectral images: A comprehensive survey. *Electronics*, 12(3):488, 2023.

[10] Sicong Liu, Daniele Marinelli, Lorenzo Bruzzone, and Francesca Bovolo. A review of change detection in multitemporal hyperspectral images: Current techniques, applications, and challenges. *IEEE Geoscience and Remote Sensing Magazine*, 7(2):140–158, 2019.

[11] Brajesh Kumar, Onkar Dikshit, Ashwani Gupta, and Manoj Kumar Singh. Feature extraction for hyperspectral image classification: A review. *International Journal of Remote Sensing*, 41(16):6248–6287, 2020.

[12] Weiwei Sun and Qian Du. Hyperspectral band selection: A review. *IEEE Geoscience and Remote Sensing Magazine*, 7(2):118–139, 2019.

[13] Erting Pan, Yong Ma, Fan Fan, Xiaoguang Mei, and Jun Huang. Hyperspectral image classification across different datasets: A generalization to unseen categories. *Remote Sensing*, 13(9):1672, 2021.

[14] Mitchell Rogers, Jacques Blanc-Talon, Martin Urschler, and Patrice Delmas. Wavelength and texture feature selection for hyperspectral imaging: a systematic literature review. *Journal of Food Measurement and Characterization*, 17(6):6039–6064, 2023.

[15] Gordon Hughes. On the mean accuracy of statistical pattern recognizers. *IEEE transactions on information theory*, 14(1):55–63, 1968.

[16] Behnood Rasti, Danfeng Hong, Renlong Hang, Pedram Ghamisi, Xudong Kang, Jocelyn Chanussot, and Jon Atli Benediktsson. Feature extraction for hyperspectral imagery: The evolution from shallow to deep: Overview and toolbox. *IEEE Geoscience and Remote Sensing Magazine*, 8(4):60–88, 2020.

[17] Craig Rodarmel and Jie Shan. Principal component analysis for hyperspectral image classification. *Surveying and Land Information Science*, 62(2):115–122, 2002.

[18] J Senthilnath, SN Omkar, V Mani, Nitin Karnwal, and PB Shreyas. Crop stage classification of hyperspectral data using unsupervised techniques. *IEEE Journal of Selected Topics in Applied Earth Observations and Remote Sensing*, 6(2):861–866, 2012.

[19] Md Palash Uddin, Md Al Mamun, and Md Ali Hossain. Pca-based feature reduction for hyperspectral remote sensing image classification. *IETE Technical Review*, 38(4):377–396, 2021.

[20] Qian Du and Harold Szu. Interference and noise adjusted principal components analysis for hyperspectral remote sensing image compression. In *Independent Component Analyses, Wavelets, Unsupervised Smart Sensors, and Neural Networks IV*, volume 6247, pages 73–84. SPIE, 2006.

[21] Guangyi Chen, Adam Krzyzak, and Shen-en Qian. Noise robust hyperspectral image classification with mnf-based edge preserving features. *Image Analysis and Stereology*, 42(2):93–99, 2023.

[22] Jun-zheng Wu, Wei-dong Yan, Wei-ping Ni, and Hui Bian. Feature extraction for hyperspectral data based on mnf and singular value decomposition. In *2013 IEEE International Geoscience and Remote Sensing Symposium-IGARSS*, pages 1430–1433. IEEE, 2013.

[23] Alberto Villa, Jocelyn Chanussot, Christian Jutten, Jon Atli Benediktsson, and Saïd Moussaoui. On the use of ica for hyperspectral image analysis. In *2009 IEEE International Geoscience and Remote Sensing Symposium*, volume 4, pages IV–97. IEEE, 2009.

[24] Jing Wang and Chein-I Chang. Independent component analysis-based dimensionality reduction with applications in hyperspectral image analysis. *IEEE transactions on geoscience and remote sensing*, 44(6):1586–1600, 2006.

[25] Nicola Falco, Jon Atli Benediktsson, and Lorenzo Bruzzone. A study on the effectiveness of different independent component analysis algorithms for hyperspectral image classification. *IEEE Journal of Selected Topics in Applied Earth Observations and Remote Sensing*, 7(6):2183–2199, 2014.

[26] Bernhard Schölkopf, Alexander Smola, and Klaus-Robert Müller. Nonlinear component analysis as a kernel eigenvalue problem. *Neural computation*, 10(5):1299–1319, 1998.

[27] Allan Aasbjerg Nielsen. Kernel maximum autocorrelation factor and minimum noise fraction transformations. *IEEE Transactions on Image Processing*, 20(3):612–624, 2010.

[28] Francis R Bach and Michael I Jordan. Kernel independent component analysis. *Journal of machine learning research*, 3(Jul):1–48, 2002.

[29] Charles M Bachmann, Thomas L Ainsworth, and Robert A Fusina. Exploiting manifold geometry in hyperspectral imagery. *IEEE transactions on Geoscience and Remote Sensing*, 43(3):441–454, 2005.

[30] Francisco José Orts Gómez, Gloria Ortega López, Ernestas Filatovas, Olga Kurasova, and Gracia Ester Martın Garzón. Hyperspectral image classification using isomap with smacof. *Informatica*, 30(2):349–365, 2019.

[31] B Uma Shankar, Saroj K Meher, and Ashish Ghosh. Wavelet-fuzzy hybridization: feature-extraction and land-cover classification of remote sensing images. *Applied Soft Computing*, 11(3):2999–3011, 2011.

[32] Sinthop Kaewpijit, Jacqueline Le Moigne, and Tarek El-Ghazawi. Automatic reduction of hyperspectral imagery using wavelet spectral analysis. *IEEE transactions on Geoscience and Remote Sensing*, 41(4):863–871, 2003.

[33] Xiangyong Cao, Jing Yao, Xueyang Fu, Haixia Bi, and Danfeng Hong. An enhanced 3-d discrete wavelet transform for hyperspectral image classification. *IEEE Geoscience and Remote Sensing Letters*, 18(6):1104–1108, 2020.

[34] Nadia Zikiou, Mourad Lahdir, and David Helbert. Hyperspectral image classification using graph-based wavelet transform. *International journal of remote sensing*, 41(7):2624–2643, 2020.

[35] Arati Paul, Ahana Kundu, Nabendu Chaki, Dibyendu Dutta, and CS Jha. Wavelet enabled convolutional autoencoder based deep neural network for hyperspectral image denoising. *Multimedia tools and applications*, pages 1–27, 2022.

[36] Wenhui Guo, Guixun Xu, Baodi Liu, and Yanjiang Wang. Hyperspectral image classification using cnn-enhanced multi-level haar wavelet features fusion network. *IEEE Geoscience and Remote Sensing Letters*, 19:1–5, 2022.

[37] Wei Li, Fubiao Feng, Hengchao Li, and Qian Du. Discriminant analysis-based dimension reduction for hyperspectral image classification: A survey of the most recent advances and an experimental comparison of different techniques. *IEEE Geoscience and Remote Sensing Magazine*, 6(1):15–34, 2018.

[38] Akin Ozdemir and Kemal Polat. Deep learning applications for hyperspectral imaging: a systematic review. *Journal of the Institute of Electronics and Computer*, 2(1):39–56, 2020.

[39] Junhai Zhai, Sufang Zhang, Junfen Chen, and Qiang He. Autoencoder and its various variants. In *2018 IEEE international conference on systems, man, and cybernetics (SMC)*, pages 415–419. IEEE, 2018.

[40] Yaoming Cai, Zijia Zhang, Zhihua Cai, Xiaobo Liu, and Xinwei Jiang. Hypergraph-structured autoencoder for unsupervised and semisupervised classification of hyperspectral image. *IEEE Geoscience and Remote Sensing Letters*, 19:1–5, 2021.

[41] Wenbo Yu, Miao Zhang, and Yi Shen. Spatial revising variational autoencoder-based feature extraction method for hyperspectral images. *IEEE Transactions on Geoscience and Remote Sensing*, 59(2):1410–1423, 2020.

[42] Yongshan Zhang, Yang Wang, Xiaohong Chen, Xinwei Jiang, and Yicong Zhou. Spectral–spatial feature extraction with dual graph autoencoder for hyperspectral image clustering. *IEEE Transactions on Circuits and Systems for Video Technology*, 32(12):8500–8511, 2022.

[43] Mingyang Zhang, Maoguo Gong, Haibo He, and Shengqi Zhu. Symmetric all convolutional neural-network-based unsupervised feature extraction for hyperspectral images classification. *IEEE Transactions on Cybernetics*, 52(5):2981–2993, 2020.

[44] Shuyu Zhang, Meng Xu, Jun Zhou, and Sen Jia. Unsupervised spatial-spectral cnn-based feature learning for hyperspectral image classification. *IEEE Transactions on Geoscience and Remote Sensing*, 60:1–17, 2022.

[45] Muhammad Ahmad, Adil Mehmood Khan, Manuel Mazzara, Salvatore Distefano, Mohsin Ali, and Muhammad Shahzad Sarfraz. A fast and compact 3-d cnn for hyperspectral image classification. *IEEE Geoscience and Remote Sensing Letters*, 19:1–5, 2020.

[46] Murali Kanthi, T Hitendra Sarma, and C Shobha Bindu. A 3d-deep cnn based feature extraction and hyperspectral image classification. In *2020 IEEE India Geoscience and Remote Sensing Symposium (InGARSS)*, pages 229–232. IEEE, 2020.

[47] Chunyan Yu, Rui Han, Meiping Song, Caiyu Liu, and Chein-I Chang. A simplified 2d-3d cnn architecture for hyperspectral image classification based on spatial–spectral fusion. *IEEE Journal of Selected Topics in Applied Earth Observations and Remote Sensing*, 13:2485–2501, 2020.

[48] Zixian Ge, Guo Cao, Xuesong Li, and Peng Fu. Hyperspectral image classification method based on 2d–3d cnn and multibranch feature fusion. *IEEE Journal of Selected Topics in Applied Earth Observations and Remote Sensing*, 13:5776–5788, 2020.

[49] Min Zhao, Longbin Yan, and Jie Chen. Lstm-dnn based autoencoder network for nonlinear hyperspectral image unmixing. *IEEE Journal of Selected Topics in Signal Processing*, 15(2):295–309, 2021.

[50] Jinling Zhao, Lei Hu, Yingying Dong, Linsheng Huang, Shizhuang Weng, and Dongyan Zhang. A combination method of stacked autoencoder and 3d deep residual network for hyperspectral image classification. *International Journal of Applied Earth Observation and Geoinformation*, 102:102459, 2021.

[51] Qichao Liu, Liang Xiao, Jingxiang Yang, and Zhihui Wei. Cnn-enhanced graph convolutional network with pixel-and superpixel-level feature fusion for hyperspectral image classification. *IEEE Transactions on Geoscience and Remote Sensing*, 59(10):8657–8671, 2020.

[52] Wen-Shuai Hu, Heng-Chao Li, Lei Pan, Wei Li, Ran Tao, and Qian Du. Spatial–spectral feature extraction via deep convlstm neural networks for hyperspectral image classification. *IEEE Transactions on Geoscience and Remote Sensing*, 58(6):4237–4250, 2020.

[53] Ram Narayan Patro, Subhashree Subudhi, Pradyut Kumar Biswal, and Fabio Dell'acqua. A review of unsupervised band selection techniques: Land cover classification for hyperspectral earth observation data. *IEEE Geoscience and Remote Sensing Magazine*, 9(3):72–111, 2021.

[54] Chein-I Chang, Qian Du, Tzu-Lung Sun, and Mark LG Althouse. A joint band prioritization and band-decorrelation approach to band selection for hyperspectral image classification. *IEEE transactions on geoscience and remote sensing*, 37(6):2631–2641, 1999.

[55] Shrutika S Sawant and Manoharan Prabukumar. A survey of band selection techniques for hyperspectral image classification. *Journal of Spectral Imaging*, 9, 2020.

[56] Buyun Xu, Xihai Li, Weijun Hou, Yiting Wang, and Yiwei Wei. A similarity-based ranking method for hyperspectral band selection. *IEEE Transactions on Geoscience and Remote Sensing*, 59(11):9585–9599, 2021.

[57] Chein-I Chang, Yi-Mei Kuo, Shuhan Chen, Chia-Chen Liang, Kenneth Yeonkong Ma, and Peter Fuming Hu. Self-mutual information-based band selection for hyperspectral image classification. *IEEE Transactions on Geoscience and Remote Sensing*, 59(7):5979–5997, 2020.

[58] Peifeng Su, Sasu Tarkoma, and Petri KE Pellikka. Band ranking via extended coefficient of variation for hyperspectral band selection. *Remote Sensing*, 12(20):3319, 2020.

[59] Gang Li, Shuangshuang Ma, Ke Li, Mei Zhou, and Ling Lin. Band selection for heterogeneity classification of hyperspectral transmission images based on multi-criteria ranking. *Infrared Physics & Technology*, 125:104317, 2022.

[60] Adolfo MartÍnez-UsÓMartinez-Uso, Filiberto Pla, José Martínez Sotoca, and Pedro García-Sevilla. Clustering-based hyperspectral band selection using information measures. *IEEE Transactions on Geoscience and Remote Sensing*, 45(12):4158–4171, 2007.

[61] K Kishore Raju, GP Saradhi Varma, and D Rajya Lakshmi. Spatial residual clustering and entropy based ranking for hyperspectral band selection. *European Journal of Remote Sensing*, 53:82–92, 2020.

[62] Ibrahim Delibasoglu and Mufit Cetin. Hyperspectral band selection using structural information via hierarchical clustering. *Journal of Applied Remote Sensing*, 13(1):014526–014526, 2019.

[63] Weiwei Sun, Jiangtao Peng, Gang Yang, and Qian Du. Correntropy-based sparse spectral clustering for hyperspectral band selection. *IEEE Geoscience and Remote Sensing Letters*, 17(3):484–488, 2019.

[64] Qi Wang, Qiang Li, and Xuelong Li. A fast neighborhood grouping method for hyperspectral band selection. *IEEE Transactions on Geoscience and Remote Sensing*, 59(6):5028–5039, 2020.

[65] Yulei Tan, Laijun Lu, Lorenzo Bruzzone, Renchu Guan, Zhiyong Chang, and Chen Yang. Hyperspectral band selection for lithologic discrimination and geological mapping. *IEEE Journal of Selected Topics in Applied Earth Observations and Remote Sensing*, 13:471–486, 2020.

[66] Jun Wang, Chang Tang, Zhenglai Li, Xinwang Liu, Wei Zhang, En Zhu, and Lizhe Wang. Hyperspectral band selection via region-aware latent features fusion based clustering. *Information Fusion*, 79:162–173, 2022.

[67] Yuan Yuan, Guokang Zhu, and Qi Wang. Hyperspectral band selection by multitask sparsity pursuit. *IEEE Transactions on Geoscience and Remote Sensing*, 53(2):631–644, 2014.

[68] Qi Wang, Fahong Zhang, and Xuelong Li. Hyperspectral band selection via optimal neighborhood reconstruction. *IEEE Transactions on Geoscience and Remote Sensing*, 58(12):8465–8476, 2020.

[69] Weizhao Chen, Zhijing Yang, Jinchang Ren, Jiangzhong Cao, Nian Cai, Huimin Zhao, and Peter Yuen. Mimn-dpp: Maximum-information and minimum-noise determinantal point processes for unsupervised hyperspectral band selection. *Pattern Recognition*, 102:107213, 2020.

[70] Shrutika Sawant and Prabukumar Manoharan. Hyperspectral band selection based on metaheuristic optimization approach. *Infrared Physics & Technology*, 107:103295, 2020.

[71] Haishi Zhao, Lorenzo Bruzzone, Renchu Guan, Fengfeng Zhou, and Chen Yang. Spectral-spatial genetic algorithm-based unsupervised band selection for hyperspectral image classification. *IEEE Transactions on Geoscience and Remote Sensing*, 59(11):9616–9632, 2021.

[72] Yuting Wan, Chao Chen, Ailong Ma, Liangpei Zhang, Xunqiang Gong, and Yanfei Zhong. Adaptive multi-strategy particle swarm optimization for hyperspectral remote sensing image band selection. *IEEE Transactions on Geoscience and Remote Sensing*, 2023.

[73] Shuangjiang Li and Hairong Qi. Sparse representation based band selection for hyperspectral images. In *2011 18th IEEE International Conference on Image Processing*, pages 2693–2696. IEEE, 2011.

[74] Zhixi Feng, Shuyuan Yang, Xiaolong Wei, Quanwei Gao, and Licheng Jiao. Regularized sparse band selection via learned pairwise agreement. *IEEE Access*, 8:40096–40105, 2020.

[75] Zeyang Dou, Kun Gao, Xiaodian Zhang, Hong Wang, and Lu Han. Band selection of hyperspectral images using attention-based autoencoders. *IEEE Geoscience and Remote Sensing Letters*, 18(1):147–151, 2020.

[76] Pablo Ribalta Lorenzo, Lukasz Tulczyjew, Michal Marcinkiewicz, and Jakub Nalepa. Hyperspectral band selection using attention-based convolutional neural networks. *IEEE Access*, 8:42384–42403, 2020.

[77] Jie Feng, Jiantong Chen, Qigong Sun, Ronghua Shang, Xianghai Cao, Xiangrong Zhang, and Licheng Jiao. Convolutional neural network based on bandwise-independent convolution and hard thresholding for hyperspectral band selection. *IEEE Transactions on Cybernetics*, 51(9):4414–4428, 2020.

[78] Rui Zhang and Jianwen Ma. Feature selection for hyperspectral data based on recursive support vector machines. *International Journal of Remote Sensing*, 30(14):3669–3677, 2009.

[79] Radhesyam Vaddi and Prabukumar Manoharan. Cnn based hyperspectral image classification using unsupervised band selection and structure-preserving spatial features. *Infrared Physics & Technology*, 110:103457, 2020.

[80] Jie Feng, Di Li, Jing Gu, Xianghai Cao, Ronghua Shang, Xiangrong Zhang, and Licheng Jiao. Deep reinforcement learning for semisupervised hyperspectral band selection. *IEEE Transactions on Geoscience and Remote Sensing*, 60:1–19, 2021.

[81] Liu Zhang, Yaoguang Wei, Jincun Liu, Jianwei Wu, and Dong An. A hyperspectral band selection method based on sparse band attention network for maize seed variety identification. *Expert Systems with Applications*, 238:122273, 2024.

[82] Utpal Nandi, Swalpa Kumar Roy, Danfeng Hong, Xin Wu, and Jocelyn Chanussot. Tattmsrecnet: Triplet-attention and multiscale reconstruction network for band selection in hyperspectral images. *Expert Systems with Applications*, 212:118797, 2023.

[83] Weiwei Sun, Jiangtao Peng, Gang Yang, and Qian Du. Fast and latent low-rank subspace clustering for hyperspectral band selection. *IEEE Transactions on Geoscience and Remote Sensing*, 58(6):3906–3915, 2020.

[84] Jie Feng, Zhanwei Ye, Shuai Liu, Xiangrong Zhang, Jiantong Chen, Ronghua Shang, and Licheng Jiao. Dual-graph convolutional network based on band attention and sparse constraint for hyperspectral band selection. *Knowledge-Based Systems*, 231:107428, 2021.

[85] Shrutika S Sawant and Prabukumar Manoharan. Unsupervised band selection based on weighted information entropy and 3d discrete cosine transform for hyperspectral image classification. *International Journal of Remote Sensing*, 41(10):3948–3969, 2020.

[86] Anurag Goel and Angshul Majumdar. K-means embedded deep transform learning for hyperspectral band selection. *IEEE Geoscience and Remote Sensing Letters*, 19:1–5, 2022.

[87] Mohammad Esmaeili, Dariush Abbasi-Moghadam, Alireza Sharifi, Aqil Tariq, and Qingting Li. Hyperspectral image band selection based on cnn embedded ga (cnnega). *IEEE Journal of Selected Topics in Applied Earth Observations and Remote Sensing*, 16:1927–1950, 2023.

[88] Rolf Adams and Leanne Bischof. Seeded region growing. *IEEE Transactions on pattern analysis and machine intelligence*, 16(6):641–647, 1994.

[89] C Jaspin Jeba Sheela and GJMT Suganthi. Morphological edge detection and brain tumor segmentation in magnetic resonance (mr) images based on region growing and performance evaluation of modified fuzzy c-means (fcm) algorithm. *Multimedia Tools and Applications*, 79:17483–17496, 2020.

[90] Rajeshwari S Patil and Nagashettappa Biradar. Improved region growing segmentation for breast cancer detection: progression of optimized fuzzy classifier. *International journal of intelligent computing and cybernetics*, 13(2):181–205, 2020.

[91] K Vijila Rani, G Sumathy, LK Shoba, P Josephin Shermila, and M Eugine Prince. Radon transform-based improved single seeded region growing segmentation for lung cancer detection using ampwsvm classification approach. *Signal, Image and Video Processing*, pages 1–10, 2023.

[92] Muhamad Farid Ramli and Khairul Nizam Tahar. Homogeneous tree height derivation from tree crown delineation using seeded region growing (srg) segmentation. *Geo-Spatial Information Science*, 23(3):195–208, 2020.

[93] Sun Xianchen, Wang Baoyun, and Liu Kunxiang. Dem and valley segmentation in remote sensing image based on region growing algorithm. In *Journal of Physics: Conference Series*, volume 1693, page 012174. IOP Publishing, 2020.

[94] Leila Hashemi-Beni and Asmamaw A Gebrehiwot. Flood extent mapping: An integrated method using deep learning and region growing using uav optical data. *IEEE Journal of Selected Topics in Applied Earth Observations and Remote Sensing*, 14:2127–2135, 2021.

[95] Jingdao Chen, Zsolt Kira, and Yong K Cho. Lrgnet: learnable region growing for class-agnostic point cloud segmentation. *IEEE Robotics and Automation Letters*, 6(2):2799–2806, 2021.

[96] Yonghao Xu and Pedram Ghamisi. Region-growing fully convolutional networks for hyperspectral image classification with point-level supervision. In *CIKM Workshops*, 2021.

[97] Jianyu Gu and Russell G Congalton. Individual tree crown delineation from uas imagery based on region growing by over-segments with a competitive mechanism. *IEEE Transactions on Geoscience and Remote Sensing*, 60:1–11, 2021.

[98] Yuxian Wang, Kui Li, Linlin Xu, Qian Wei, Fang Wang, and Ye Chen. A depthwise separable fully convolutional resnet with convcrf for semisupervised hyperspectral image classification. *IEEE Journal of Selected Topics in Applied Earth Observations and Remote Sensing*, 14:4621–4632, 2021.

[99] Nathan Magro, Alexandra Bonnici, and Stefania Cristina. Hyperspectral image segmentation for paint analysis. In *2021 IEEE International Conference on Image Processing (ICIP)*, pages 1374–1378. IEEE, 2021.

[100] Yonghao Xu and Pedram Ghamisi. Consistency-regularized region-growing network for semantic segmentation of urban scenes with point-level annotations. *IEEE Transactions on Image Processing*, 31:5038–5051, 2022.

[101] Guansheng Yin, Jianguo Gao, Jianmin Gao, Chang Li, Mingzhu Jin, Minghui Shi, Hongliang Tuo, and Pengfei Wei. Crack identification method of highway tunnel based on image processing. *Journal of Traffic and Transportation Engineering (English Edition)*, 10(3):469–484, 2023.

[102] Zihan Liu, Hongming Zhang, Liang Dong, Zhitong Sun, Shufang Wu, Biao Zhang, Linlin Yuan, Zhenfei Wang, and Qimeng Jia. An optimised region-growing algorithm for extraction of the loess shoulder-line from dems. *ISPRS International Journal of Geo-Information*, 12(4):140, 2023.

[103] Ioannis Kotaridis and Maria Lazaridou. Remote sensing image segmentation advances: A meta-analysis. *ISPRS Journal of Photogrammetry and Remote Sensing*, 173:309–322, 2021.

[104] Shima Rafiei, Nader Karimi, Behzad Mirmahboub, Kayvan Najarian, Banafsheh Felfeliyan, Shadrokh Samavi, and SM Reza Soroushmehr. Liver segmentation in abdominal ct images using probabilistic atlas and adaptive 3d region growing. In *2019 41st annual international conference of the IEEE engineering in medicine and biology society (EMBC)*, pages 6310–6313. IEEE, 2019.

[105] Yuhu Shi, Min Li, and Weiming Zeng. Margm: A multi-subjects adaptive region growing method for group fmri data analysis. *Biomedical Signal Processing and Control*, 69:102882, 2021.

[106] Hyperspectral remote sensing scenes. `http://www.ehu.eus/ccwintco/index.php/Hyperspectral_Remote_Sensing_Scenes`. Accessed 11 September 2023.

[107] NERC Airborne Research Facility. Nerc-arf 2014_288 - rg13_06 flight: Airborne remote sensing measurements. Centre for Environmental Data Analysis, 2020. Accessed on 21 July 2020.

[108] Mirko Paolo Barbato, Paolo Napoletano, Flavio Piccoli, and Raimondo Schettini. Unsupervised segmentation of hyperspectral remote sensing images with superpixels. *Remote Sensing Applications: Society and Environment*, 28:100823, 2022.

[109] Ámbar Pérez-García, Mercedes E Paoletti, Juan M Haut, and José F López. Novel spectral loss function for unsupervised hyperspectral image segmentation. *IEEE Geoscience and Remote Sensing Letters*, 2023.

[110] Dorin Comaniciu and Peter Meer. Mean shift: A robust approach toward feature space analysis. *IEEE Transactions on pattern analysis and machine intelligence*, 24(5):603–619, 2002.

[111] Spectral python (spy): Python module for hyperspectral image processing. `https://github.com/spectralpython/spectral/tree/master?tab=readme-ov-file`. Accessed 15 January 2024.

[112] Jannick Kuester, Wolfgang Gross, and Wolfgang Middelmann. 1d-convolutional autoencoder based hyperspectral data compression. *The International Archives of the Photogrammetry, Remote Sensing and Spatial Information Sciences*, 43:15–21, 2021.